Journal of Sound and Vibration (1999) **220**(5), 861–903
Article No. jsvi.1998.1988, available online at http://www.idealibrary.com.on IDEAL

SIMULATION OF THE DYNAMIC BEHAVIOUR OF SINGLE AND MULTI-STAGE GEARED SYSTEMS WITH SHAPE DEVIATIONS AND MOUNTING ERRORS BY USING A SPECTRAL METHOD

J. P. Raclot and P. Velex

Laboratoire de Mécanique des Contacts UMR CNRS 5514, *INSA de Lyon*, *Bâtiment* 113 20 *avenue Albert Einstein*, 69621 *Villeurbanne Cédex*, *France*

(*Received* 14 *February* 1997, *and in final form* 24 *September* 1998)

A mathematical model is introduced for simulating the contributions of shape deviations and mounting errors to the dynamic behaviour of single and multi-mesh geared systems. Parametric and external excitations are characterized by using the contact conditions for both rigid and deformable bodies. The corresponding excitation functions cover a broad range of frequencies which can hardly be taken into account by time-step integration methods. To this end, an iterative spectral method is extended to multi-mesh systems submitted to multi-frequency excitations. The basic features of the method are detailed and its range of validity is discussed by comparing its results with those given by a time-step method combined to a normal contact algorithm. Finally, the potential of the numerical procedure is illustrated by analyzing the dynamic couplings in two different double-stage unit architectures.

1. INTRODUCTION

As illustrated by the reviews of Özgüven and Houser [1], Blankenship and Singh [2], and Velex [3], the gear dynamics literature presents a large variety of models mostly focused on single stage trains. Early research efforts on multi-mesh systems comprise the works of Tordion and Gauvin [4] on parametric instabilities, Iida *et al*. [5, 6], Choy *et al*. [7], Velex and Saada [8] who analyzed the modal characteristics of coupled torsional–flexural vibrations in two-stage systems. The linear behaviour of double mesh gear sets has been investigated by Umezawa *et al*. [9], Velex and Saada [10], Linke and Börner [11] who considered time-varying mesh stiffnesses and analyzed the possible interactions between each mesh for several gear arrangements. The excitations caused by shape deviations have been introduced by Rashidi and Krantz [12] on a split torque system and Kahraman [13] on various double stage units, the authors determined the mode shapes and the forced responses to parametric and external excitations. Parallel developments

0022–460X/99/100861 + 43 $30.00/0

have been conducted on planetary gear train modellings by Kahraman [14], Saada and Velex [15], and Velex and Flamand [16] where additional recent references about planetary gear dynamic models can be found. Non-linear behaviours of lightly loaded and/or lightly damped reverse-idler gear pairs with concurrent clearances have been analyzed by Rook and Singh [17]. Vinayak *et al*. [18] extended the formulation of Blankenship and Singh [19] for single mesh systems to double stage units. The state equations are solved by using a multi-term harmonic balance method and both linear time invariant (LTI) and linear time-varying (LTV) coefficient systems are considered. In two more recent papers, Vinayak and Singh [20, 21] introduced the influence of gear blank compliances on LTI multi-mesh drive models.

The literature review reveals that most of the multi-stage simulations use simplified and global excitation models mainly based on transmission errors introduced as some displacement functions at the mesh interfaces. As discussed in reference [22], transmission error under load is essentially bidimensional in nature and combines rigid-body displacements and deflections whose contributions should be clearly separated. Consequently, it is believed that the problem of contact and force couplings between mating flanks with real deviations and geometrical errors in multi-mesh gear dynamics has yet to be addressed. From a numerical point of view, the major difficulty comes from the scale differences in characteristic dimensions (from a few microns for a tooth shape defect to approximately a meter for a shaft length) and in characteristic periods (from a fraction of the tooth passing period to the system basic period which is much larger).

The present paper is an attempt to bridge this gap, its main objectives are: (i) to present a modular approach based on a finite element procedure (mass, stiffness matrices and elementary second members) valid for single and multi-mesh systems; (ii) to consider a more refined 3D tooth contact model than the ones used in the multi-stage dynamic models of the literature and to include actual shape deviations and mounting errors on all pinions and gears; (iii) to extend the iterative spectral method originally developed by Perret-Liaudet and Sabot [23], Perret-Liaudet [24], and Perret-Liaudet and Sabot [25] in order to account for single and double stage units with realistic geometrical errors generating broad band external and parametric excitations; (iv) to validate the proposed resolution technique by comparing some of its results to those given by a time-step integration scheme; and (v) to illustrate the potential of the methodology by some practical applications on double stage systems with a combination of usual shape deviations and errors.

2. STATE OF REFERENCE

Following Velex and Maatar [22], rigid-body motions define the state of reference for the multi-mesh dynamic formulation. Each potential line of contact on all base planes is discretized in elementary cells centred in M_i, one potential point of contact. In order to simulate the contribution of defects and shape modifications, a discrete normal deviation $e_s(M_i)$, where subscript s refers to stage

s, is attributed to each cell of the grid. With M^* denoting a non-singular point of contact on the base plane of stage s, rigid-body kinematics imposes

$$Rb_{gs}\Omega_{gs} + Rb_{ps}\Omega_{ps} + \varepsilon_s \dot{e}_s(M^*)/\cos\beta_{bs} = 0, \tag{1}$$

with

$$\dot{e}_s(M^*) = (\mathrm{d}/\mathrm{d}t)\{\max(e_s(M_i))\}, \tag{2}$$

and $\varepsilon_s = +1$ for a pinion positive rotation, $\varepsilon_s = -1$ for a pinion negative rotation. Ω_{ps}, Ω_{gs} are the rigid-body angular velocities of the pinion and gear of stage s, β_{bs} is the base helix angle of stage s and Rb_{ps}, Rb_{gs} are the base radii of the pinion and the gear of stage s. (A list of notation is given in the Appendix.)

Upon assuming that friction forces on tooth flanks can be neglected compared to normal loads and keeping first order terms only (see reference [22] for more details), the Kinetic Energy Theorem yields the relation between input and output torques (C_{in}, C_{out}) and angular velocities (Ω_{in}, Ω_{out}) as

$$\sum_{k}^{Nshaft} J_k \dot{\Omega}_k \Omega_k = C_{in}\Omega_{in} + C_{out}\Omega_{out}, \tag{3}$$

where J_k represents the polar moment of inertia of the shaft line k and *Nshaft* is the number of shaft lines of the drive.

In practice, Ω_{in} and C_{out} are imposed and the remaining unknowns can be determined by using equations (1) and (3). Mechanical arrangements with multiple inputs and outputs can be taken into account by the proposed formulation but the numerical applications in this paper are kept limited to the systems with a single input and output.

3. DEFORMED STATE

3.1. GEAR ELEMENTS

The model is an extension of the formulation proposed by Velex and Maatar [22] for single stage units. The fundamental differences are due to the different orientations of the pinion-gear centre-lines and the introduction of several frames of reference for the degree-of-freedom definition. Each pinion or gear is assimilated to a rigid cylinder with all six degrees of freedom: i.e., three translations and three rotations which are considered as small quantities in the vicinity of rigid-body motions. For generality, the following conventions are established: (a) the degrees of freedom attributed to the pinion and the gear of stage 1 are defined with respect to the frame (R1) such that (O_{p1}, s_1) is along the centre line of stage 1 (O_{p1}, O_{g1}); (b) the degree-of-freedom vector attributed to the pinion of stage s is defined in the same frame of reference as the degree-of-freedom vector of the gear of stage $s-1$; (c) the degree-of-freedom vector of the gear of stage s is defined in the frame linked to the pinion-gear centre line of stage s.

Upon isolating a given pinion-gear pair, the most general situation, can be represented as shown in Figure 1. The deformable part of the pinion-gear system is assimilated to a Winckler type foundation formed by a series of lumped

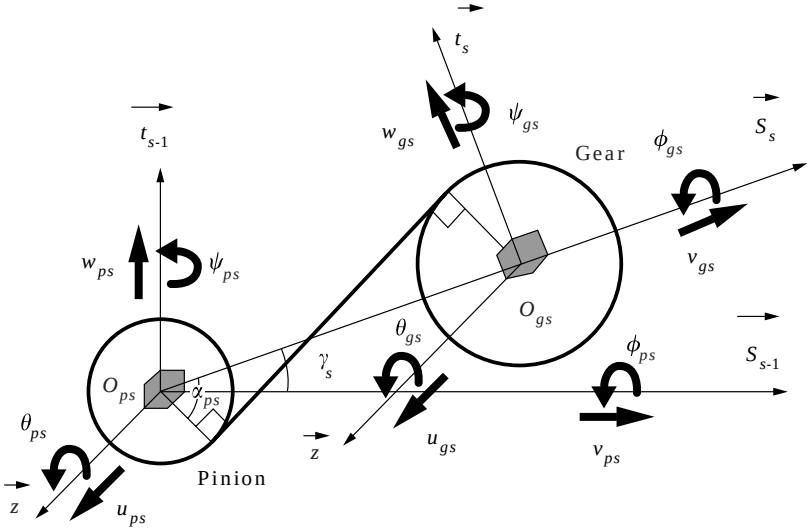

Figure 1. Degree-of-freedom definition (positive rotation of pinion).

stiffnesses k_{si} distributed along the potential lines of contact on the theoretical base planes [19, 22] (see Figure 2). Such a ''thin-slice'' approach does not include any convective effect and can hardly give the exact tooth load distribution especially near the flank edges. However, comparisons with experimental data on narrow-faced gears [22, 32, 33] indicate that the predicted transmission errors are correct while tooth load distributions remain acceptable for moderate defect amplitudes. Mesh stiffnesses k_{si} can be determined by various methods (finite elements, Weber–Banaschek formulae [34], ISO/DIS 6336 formula [35], . . .). For the isolated spur or helical gear pair defined in Table 1, quasi-static transmission errors under load (1500 Nm on pinion) for ideal geometries have been calculated

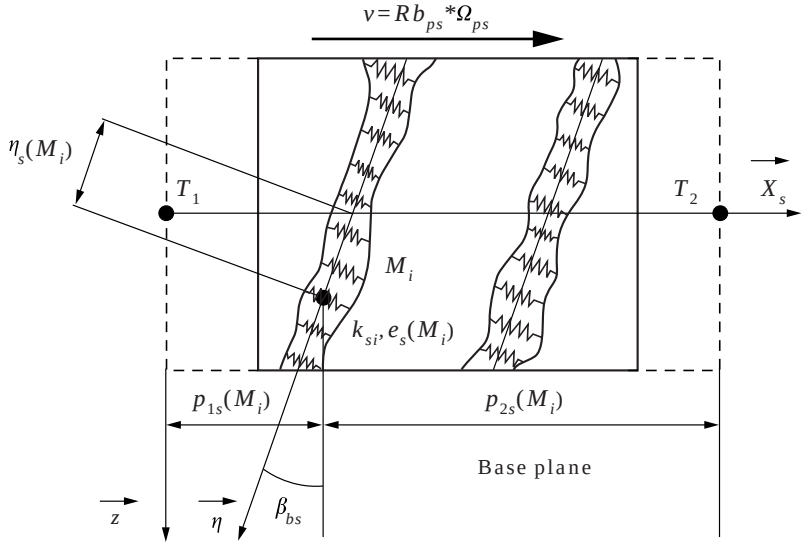

Figure 2. Mesh stiffness modelling.

TABLE 1
Gear data

	Pinion	Gear
Number of teeth (Z_1, Z_2)	27	63
Width (mm)	72 (spur) or 36 (helical)	
Module (mm)	4	
Pressure angle (deg)	20	
Helix angle (deg)	0 (spur) or 16 (helical)	
Addendum coefficient	1·0	1·0
Dedendum coefficient	1·4	1·4
Shift profile coefficient	0·0	0·0

by using an extended 3D tooth contact model [36] and the present "thin-slice" formulation with two different stiffness modellings. Such a simplified approach is certainly not as accurate as 3D contact models at the local scale (edge effects, butressing effects, . . .) but the results in Figure 3 show that the proposed mesh interface model can be considered as a good compromise for transmission error calculations. Extensions to gear dynamics is straightforward and, moreover, the time-dependent rocking moments at gear centres appear naturally in the state equations contrary to the classical formulations based on a single mesh stiffness (even if it is deduced from sophisticated tooth contact models).

In the present paper, the potential of the model together with the interest and limitations of the iterative spectral method are illustrated by using a uniform distribution of mesh stiffness per unit contact length derived from the Draft Standard ISO/DIS 6336 formula.

The deflection at M_i, a potential point of contact of stage s is equivalent to the normal approach with respect to the state of reference minus the initial gap $\delta e_s(M_i)$ and can be expressed as

$$\Delta_s(M_i) = {}^{\mathrm{T}}V_s(M_i)q_s - \delta e_s(M_i) \tag{4}$$

submitted to the constraint

$$\Delta_s(M_i) \succ 0 \tag{5}$$

for an actual point of contact, while $\Delta_s(M_i) \leqslant 0$ implies that M_i should be excluded off the contact lines.

$\delta e_s(M_i) = e_s(M^*) - e_s(M_i)$ represents the equivalent normal deviation at M_i and accounts for geometrical errors and deviations possibly produced by tooth flank modifications, misalignments, eccentricities, ... q_s is the degree-of-freedom vector of stage s defined as

$$q_s = {}^{\mathrm{T}}(u_{ps}, v_{ps}, w_{ps}, \phi_{ps}, \psi_{ps}, \theta_{ps}, u_{gs}, v_{gs}, w_{gs}, \phi_{gs}, \psi_{gs}, \theta_{gs}). \tag{6}$$

$V_s(M_i)$ is the so-called structure vector relative to an isolated stage s whose components are

$$
\begin{aligned}
{}^{\mathrm{T}}V_s(M_i) = \{&\sin\beta_{bs}, \cos\beta_{bs}\sin\kappa_s, \varepsilon_s\cos\beta_{bs}\cos\kappa_s,\\
&\varepsilon_s Rb_{ps}\sin\beta_{bs}\sin\kappa_s + \varepsilon_s[p_{1s}(M_i)\sin\beta_{bs} - \eta_s(M_i)]\cos\kappa_s,\\
&-Rb_{ps}\sin\beta_{bs}\cos\kappa_s - [p_{1s}(M_i)\sin\beta_{bs} - \eta_s(M_i)]\sin\kappa_s,\\
&\varepsilon_s Rb_{ps}\cos\beta_{bs}, \quad -\sin\beta_{bs}, \quad -\cos\beta_{bs}\sin\alpha_{ps}, \quad -\varepsilon_s\cos\beta_{bs}\cos\alpha_{ps},\\
&-\varepsilon_s Rb_{gs}\sin\beta_{bs}\sin\alpha_{ps} + \varepsilon_s[p_{2s}(M_i)\sin\beta_{bs} + \eta_s(M_i)]\cos\alpha_{ps},\\
&-Rb_{gs}\sin\beta_{bs}\cos\alpha_{ps} - [p_{2s}(M_i)\sin\beta_{bs} + \eta_s(M_i)]\sin\alpha_{ps}, \quad \varepsilon_s Rb_{gs}\cos\beta_{bs}\}
\end{aligned}
\tag{7}
$$

with $\kappa_s = \alpha_{ps} - \varepsilon_s\gamma_s$, and $p_{1s}(M_i)$ the distance from a potential point of contact M_i to pinion, $p_{2s}(M_i)$ the distance from a potential point of contact M_i to gear, and $\eta_s(M_i)$ the co-ordinate of a potential point of contact M_i along the line of contact (origin at the intersection of T_1T_2 and the line of contact (see Figure 2)).

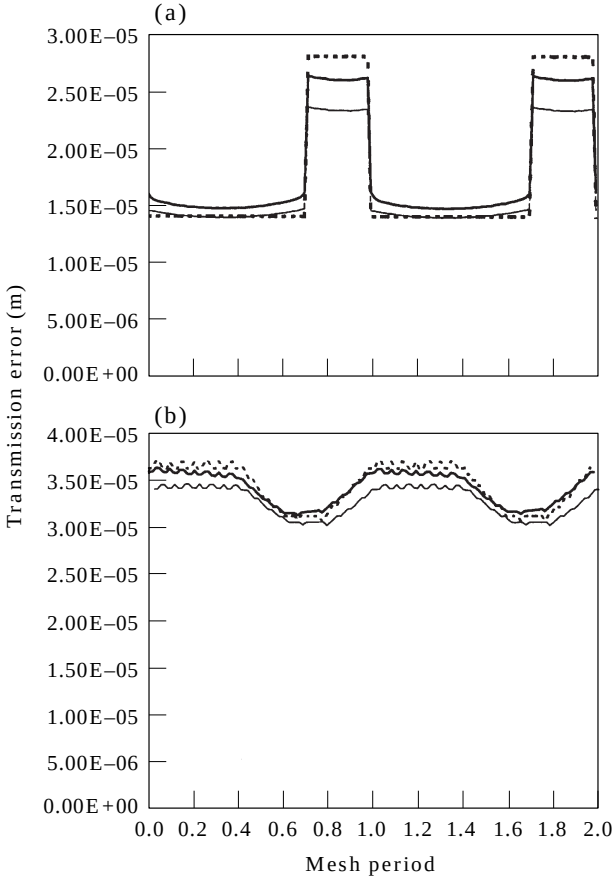

Figure 3. Quasi-static transmission errors under load by a "thin-slice" model and a 3-D model with convective effects. (a) Spur gear example; (b) helical gear example. ——, Weber–Banaschek; ——, from ISO; ——, 3D model.

In the rest of the text, equation (4) is simplified by considering the average structure vector V_{ms}, defined as

$$V_{ms} = \frac{1}{Tms} \int_0^{Tms} \left(\frac{1}{Ncs(t)} \sum_i^{Ncs(t)} V_s(M_i) \right) \mathrm{d}t, \tag{8}$$

where Tms is the mesh period of stage s and $Ncs(t)$ represents the instantaneous number of contacting cells or the number of stiffnesses in compression on the base plane of stage s. At this stage, it should be pointed out that the instantaneous number of contacting cells $Ncs(t)$ can be unknown because of a possible reduction in the actual contact radio which depends on both tooth flank deviations and actual tooth load. In such a case, $Ncs(t)$ and V_{ms} are evaluated as indicated in equation (18) of section 3.3.

For stage s, the pinion-gear pair strain energy reads

$$U_s(t) = \frac{1}{2} \sum_{i=1}^{Ncs(t)} k_{si} \Delta_s(M_i)^2, \tag{9}$$

which, upon using equations (4)–(8), gives

$$U_s(t) = \tfrac{1}{2}{}^{\mathrm{T}}q_s \left[\sum_{i=1}^{Ncs(t)} k_{si} {V_{ms}}^T V_{ms} \right] q_s - {}^{\mathrm{T}}q_s \sum_{i=1}^{Ncs(t)} k_{si} \delta e_s(M_i) V_{ms} + \frac{1}{2} \sum_{i=1}^{Ncs(t)} k_{si} \delta e_s^2(M_i) \tag{10}$$

Here

$$\left[\sum_{i=1}^{Ncs(t)} k_{si} {V_{ms}}^T V_{ms} \right] \quad \text{and} \quad \sum_{i=1}^{Ncs(t)} k_{si} \delta e_s(M_i) V_{ms}$$

are the time-dependent possibly non-linear elementary stiffness matrix and elementary excitation vector associated to stage s.

Upon neglecting second order terms and gyroscopic effects, the inertial kinetic energy of stage s is expressed as

$$\begin{aligned} T_s^o = {} & \tfrac{1}{2}[m_{ps}[\dot{u}_{ps}^2 + (\dot{v}_{ps} + S_{ps})^2 + (\dot{w}_{ps} + C_{ps})^2] + I_{ps}[\dot{\phi}_{ps}^2 + \dot{\psi}_{ps}^2] + I_{ops}[\Omega_{ps} + \dot{\theta}_{ps}]^2 \\ & + m_{gs}[\dot{u}_{gs}^2 + (\dot{v}_{gs} + S_{gs})^2 + (\dot{w}_{gs} + C_{gs})^2] + I_{gs}[\dot{\phi}_{gs}^2 + \dot{\psi}_{gs}^2] + I_{ogs}[\Omega_{gs} + \dot{\theta}_{gs}]^2], \end{aligned} \tag{11}$$

with

$$S_{p,gs} = -e_{p,gs}\Omega_{p,gs} \sin(\Omega_{p,gs}t - \lambda_{p,gs}), \qquad C_{p,gs} = e_{p,gs}\Omega_{p,gs} \cos(\Omega_{p,gs}t - \lambda_{p,gs}).$$

λ_{ps}, λ_{gs} define the angular position of the eccentricity of the pinion and gear of stage s, respectively, m_{ps}, m_{gs} are the masses, I_{ps}, I_{gs} and I_{ops}, I_{ogs} are respectively the transverse and polar moments of inertia of the pinion and the gear of stage s, and e_{ps}, e_{gs} are the eccentricities on the pinion and gear of stage s (see Figure 4).

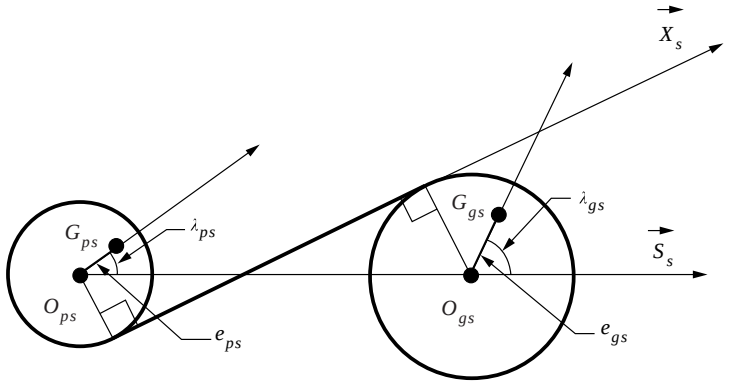

Figure 4. Eccentricities on pinion and gear.

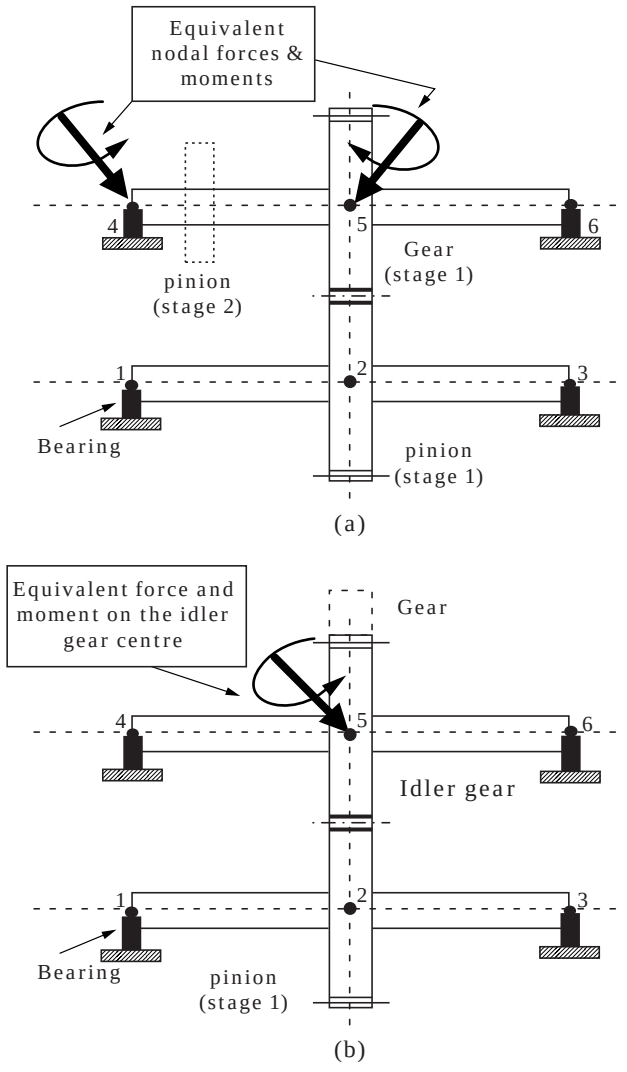

Figure 5. Auxiliary mechanical systems for quasi-static contact analyses. (a) Dual mesh systems; (b) idler gear.

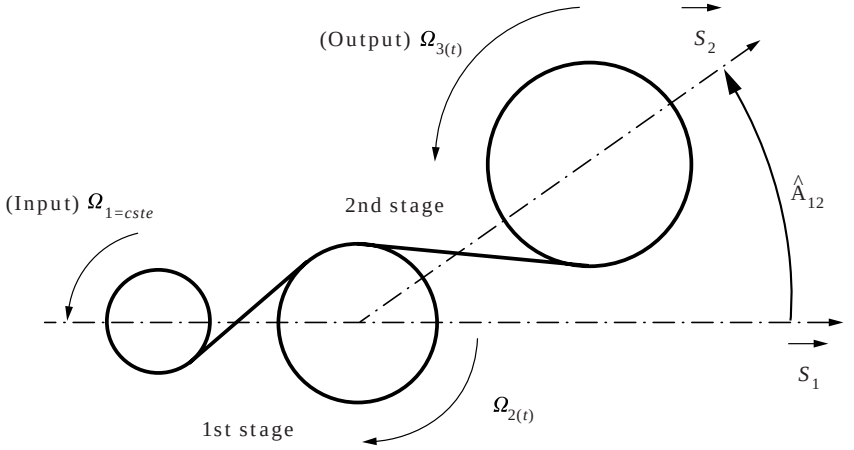

Figure 6. Reduction unit with an idler gear (type B).

Lagrange's equations lead to the following elementary mass matrix and excitation vector:

$$[M_s] = \text{diag}\,(m_{ps}, m_{ps}, m_{ps}, I_{ps}, I_{ps}, I_{ops}, m_{gs}, m_{gs}, m_{gs}, I_{gs}, I_{gs}, I_{ogs}), \tag{12}$$

$$H_s(t) = {}^{\mathrm{T}}(0, -m_{ps}\dot{C}_{ps}, -m_{ps}\dot{S}_{ps}, 0, 0, I_{ops}\dot{\Omega}_{ps}, 0, m_{gs}\dot{C}_{gs}, -m_{gs}\dot{S}_{gs}, 0, 0, I_{ogs}\dot{\Omega}_{gs}). \tag{13}$$

3.2. GLOBAL EQUATIONS

A complete drive can be decomposed into a set of pinion-gear elements, shaft elements (including axial, flexural and torsional displacements) and lumped parameter elements in order to simulate the contributions of bearings, couplings, load machines [16] . . . . After eliminating the redundant mass matrices for a pinion or a gear common to several meshes, assembly of all elementary matrices and

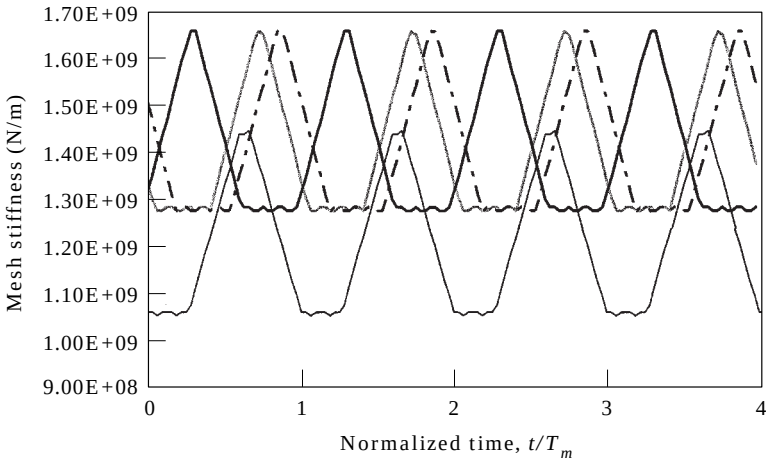

Figure 7. Influence of $\hat{A}_{12}$ on mesh stiffness functions. ——, 1st stage; ——, 2nd stage, $\hat{A}_{12}=0^\circ$, ——, 2nd stage, $\hat{A}_{12}=4^\circ$; —, 2nd stage, $\hat{A}_{12}=8^\circ$.

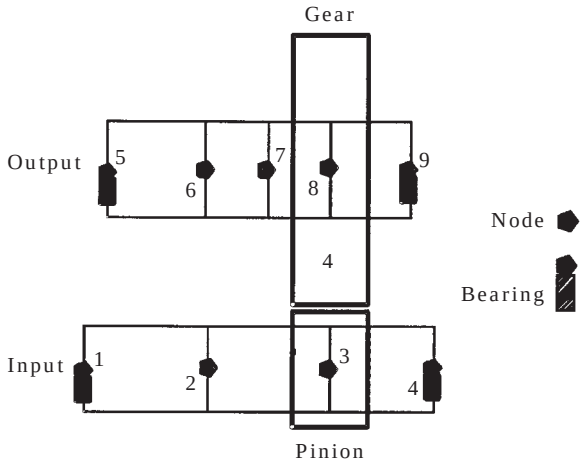

Figure 8. Simple stage drive model (54 d.o.f.).

vectors lead to the differential system valid for both reverse idler configurations and multi-stage sets:

$$[M]\ddot{X} + [C]\dot{X} + [K]X + \left[\sum_{s=1}^{Nstage} \Delta k_s(t)[G_s]\right]X$$

$$= Fo + \sum_{s=1}^{Nstage}\left[\hat{H}_s(t) + \left(\sum_{i}^{Ncs(t)} k_{si}\delta e_s(M_i)\right)\hat{V}_{ms}\right]. \tag{14}$$

Here $[M]$, $[C]$, $[K]$ are the constant mass, damping and stiffness matrices, $\hat{H}_s(t)$ and $\hat{V}_{ms}$ represent $H_s(t)$ and V_{ms} completed by zeros to the total system size, *Nstage* is the number of stages (meshes).

In equation (14), the average and time-varying parts of all mesh stiffnesses have been separated as

$$\sum_{i}^{Ncs(t)} k_{si} = k_{ms} + \Delta k_s(t), \tag{15}$$

and the following notations have been introduced:

$$[K] = [Kc] + \sum_{s}^{Nstage} k_{ms}\hat{V}_{ms}{}^{T}\hat{V}_{ms}, \qquad [G_s] = \hat{V}_{ms}{}^{T}\hat{V}_{ms}, \tag{16, 17}$$

with $[Kc]$ the constant stiffness matrix associated to the shaft-bearing-coupling system.

3.3. LINEARIZED EXCITATION FUNCTIONS

The stage equations are non-linear with time-varying (or position-varying) coefficients $\Delta k_s(t)$ and $\sum_i^{Ncs(t)} k_{si}\delta e_s(M_i)$. Solutions of such equations being very computationally intensive especially for multi-mesh systems, a simplified approach conceptually close to the one introduced by Özgüven and Houser [26] and extended by Vinayak *et al*. [18] is used. The actual excitations are approximated by their corresponding quasi-static expressions, i.e., when rigid-body rotations are close to zero. Upon neglecting the influence of long wave length defects on global load distributions, the associated linear time-averaged system (averaged over one mesh period) is solved in order to get a static solution vector $\bar{X}_o$ and the corresponding mesh forces and moments. In a second step, the

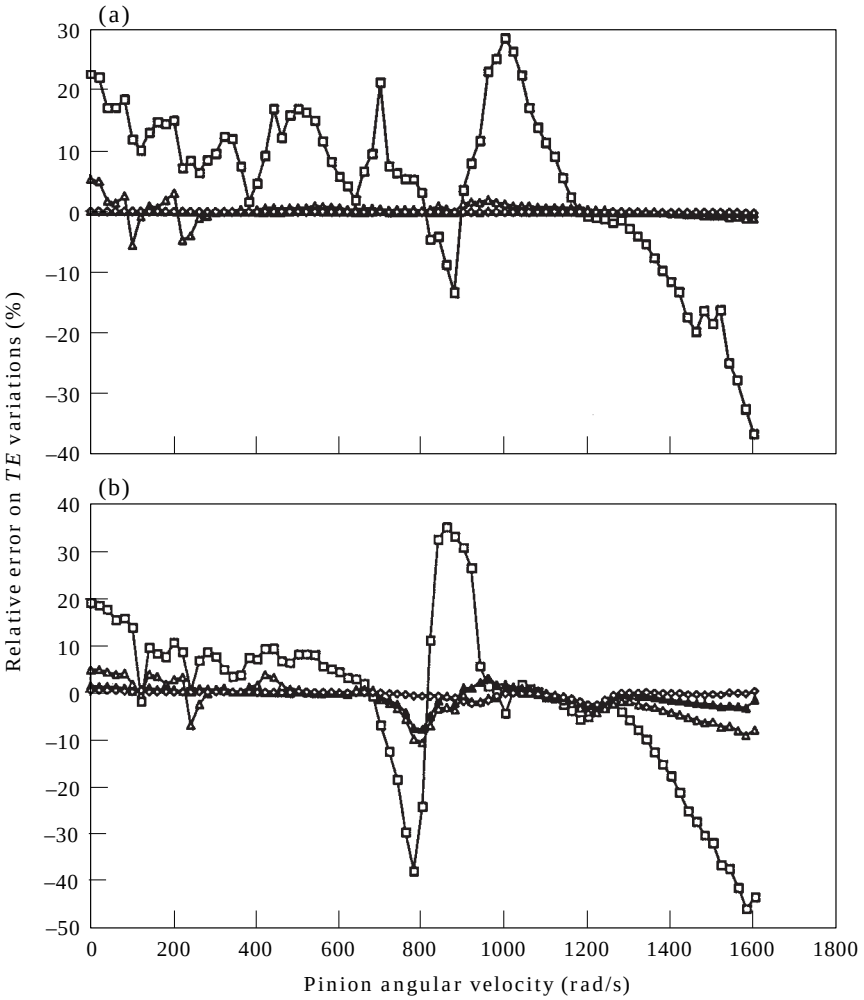

Figure 9. Comparisons between direct and Ritz methods. (a) Spur gear example; (b) helical gear example. Number of modes. —□—, 5; —△—, 10; —▲—, 15; —○—, 25.

TABLE 2

Shaft, bearing data

	Left side length (mm)	Right side length (mm)	External diameter (mm)
Input shaft	233·55	98·43	80·00
Output shaft	211·81	76·69	90·00
Bearing	For all bearings, radial stiffness $k_p = 4 \times 10^8$ N/m		

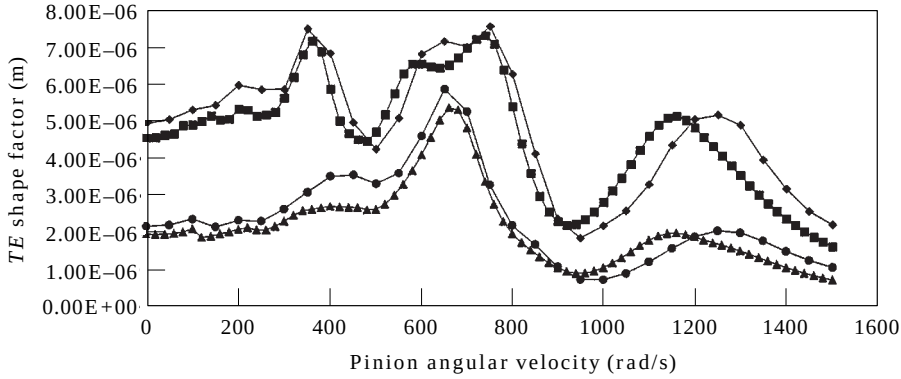

Figure 10. Evolution of TE shape factors versus pinion speed (perfect spur and helical gears). —■—, Spectral method (spur); —◆—, Newmark method (spur); —▲—, Spectral method (helical); —●—, Newmark method (helical).

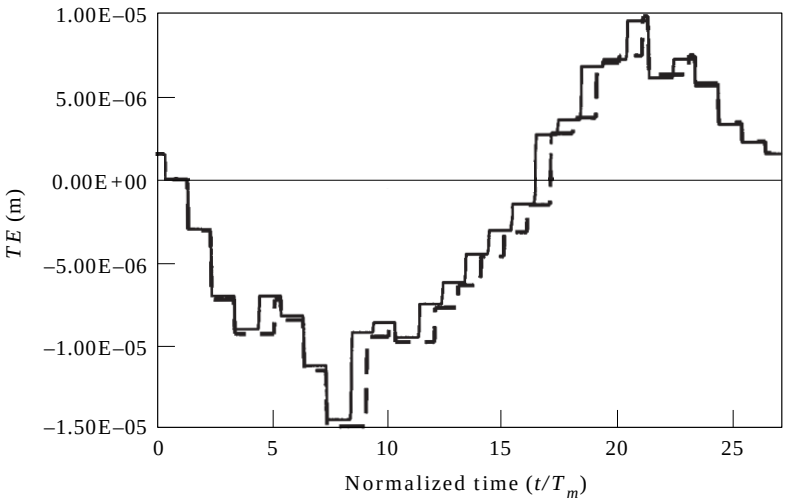

Figure 11. Pitch errors an spur (——) and helical (——) gears.

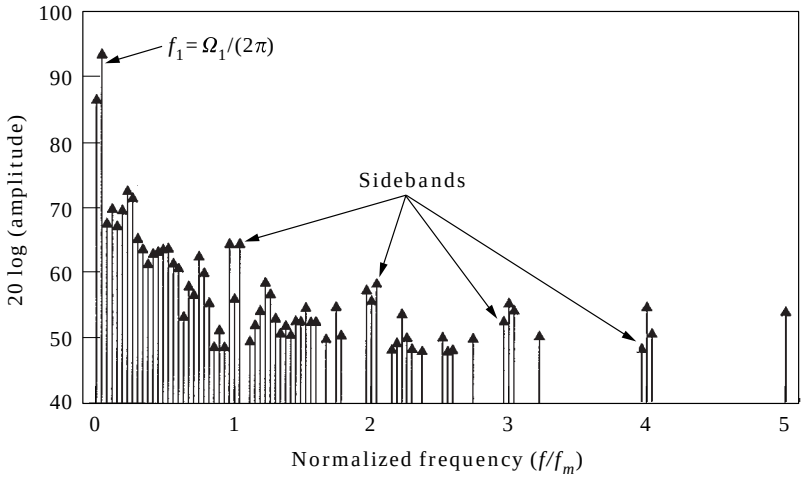

Figure 12. Spectrum of quasi-static transmission error under load (helical gear).

excitation functions generated by each individual mesh are determined by several quasi-static contact analyses (with all shape deviations and mounting errors) conducted mesh by mesh with the proper boundary conditions on forces and moments in order to account for the influence of the neighbouring pinion-gear pairs [27]. Each stage, i.e., a pinion-gear pair and its supports, is isolated and the contributions from its mechanical environment are replaced by the equivalent set of forces and moments determined by the classical formulae in rigid-body mechanics and the finite element shape functions for double stage drives. The principle is illustrated in Figure 5 for two possible configurations of double stage gear sets. In these examples, each isolated sub-system is described by the 36-degree-of-freedom model presented in reference [22] but, depending on the

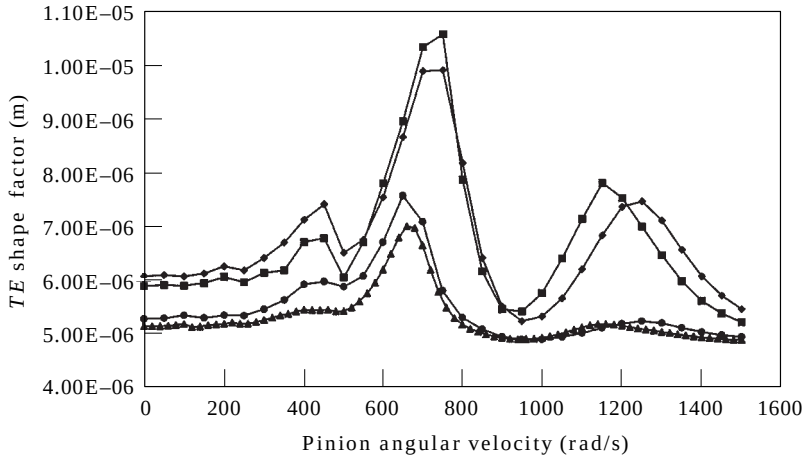

Figure 13. Comparisons between Newmark and spectral methods (pitch errors, tip reliefs). —■—, Spectral (spur); —◆—, Newmark (spur); —▲—, Spectral (helical); —●—, Newmark (helical).

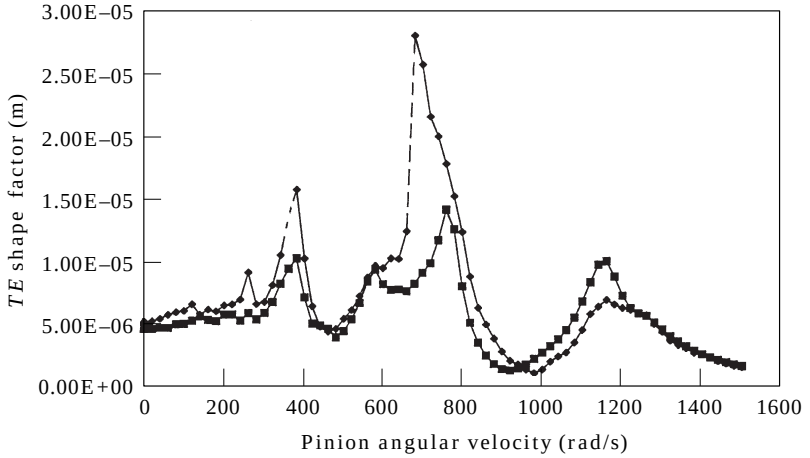

Figure 14. Comparisons between Newmark and spectral methods (perfect spur gear, damping 5%). Key as Figure 13.

complexity of the gear set, more sophisticated auxiliary models can be used if needed.

The following approximations are introduced:

$$N_{cs}(t) = \sum_{i}^{Ns(t)} \mathrm{H}(\Delta_s(M_i)) \cong \sum_{i}^{Ns(t)} \mathrm{H}(\Delta_{so}(M_i)), \tag{18}$$

$$\sum_{i}^{Ncs(t)} k_{si} = \sum_{i}^{Ns(t)} k_{si}\mathrm{H}(\Delta_s(M_i)) \cong \sum_{i}^{Ns(t)} k_{si}\mathrm{H}(\Delta_{so}(M_i)), \tag{19}$$

$$\sum_{i}^{Ncs(t)} k_{si}\delta e_s(M_i) = \sum_{i}^{Ns(t)} k_{si}\delta e_s(M_i)\mathrm{H}(\Delta_s(M_i)) \cong \sum_{i}^{Ns(t)} k_{si}\delta e_s(M_i)\mathrm{H}(\Delta_{so}(M_i)). \tag{20}$$

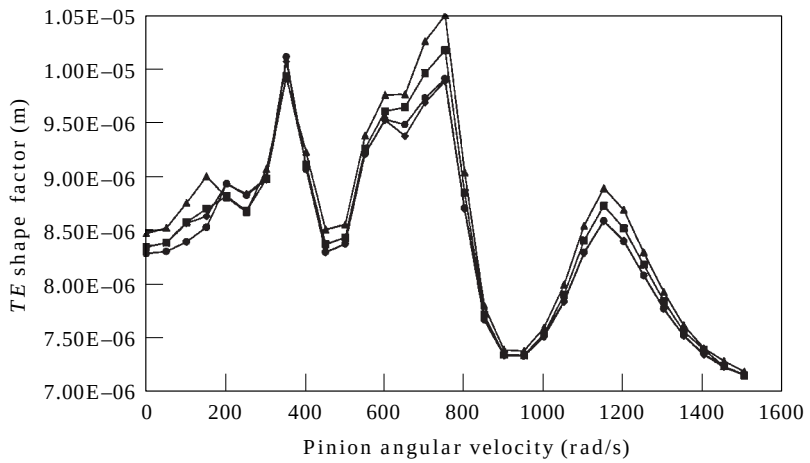

Figure 15. Influence of the number of discretization points per mesh period on dynamic transmission errors. —■—, 32 pts; —◆—, 18·963 pts; —▲—, 12 pts; —●—, 9·482 pts.

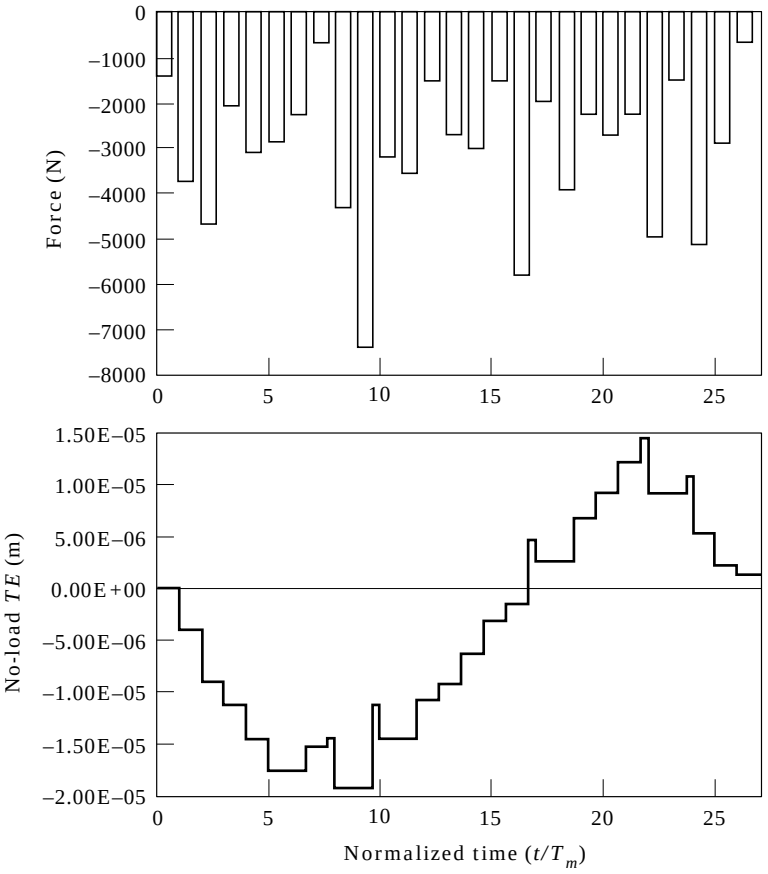

(a)

Fig. 16a.

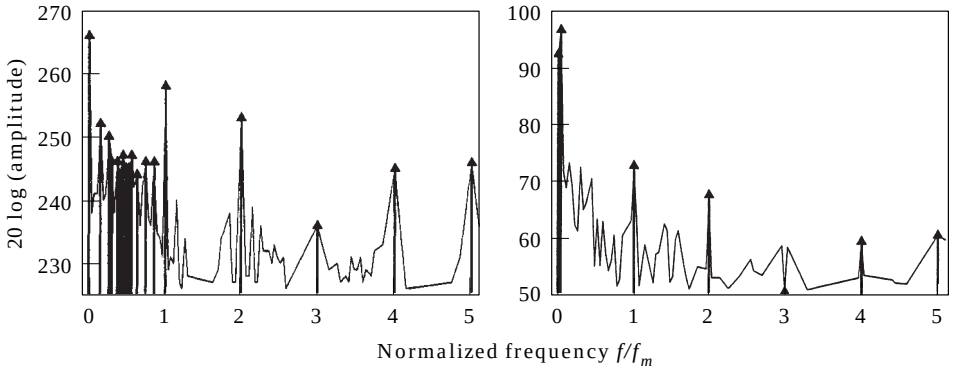

(b)

Fig. 16b.

Here H(x) is the Heaviside unit function, H(x) = 1 if $x \succ 0$, H(x) = 0 if $x \leqslant 0$, and $\Delta_{so}(M_i) = \lim \Delta_s(M_i)$ when $\Omega_{p,gs} \to 0$. Also $Ns(t)$ is the nominal (or maximum) time-varying number of contacting cells on stage s (see reference [28] for the exact expressions).

In such conditions, it is clear that the amplitude jumps caused by total contact losses cannot be simulated. However, for smoother conditions, i.e. partial contact losses, the validity of the approximation depends on the influence of the dynamic behaviour on the instantaneous contact lengths. Such partial contacts correspond to a reduced actual contact ratio, for example, due to a combination of light loads and (i) large tip reliefs which can delay the engagements, (ii) some lead modifications which can unload the tooth flank edges, etc. . . . Upon assuming that mesh stiffnesses and contact lengths are nearly proportional, a partial contact index ℓ defined as the actual average mesh stiffness to the nominal mesh stiffness ratio at low speed ("nominal" refers to a full contact from engagement to the end

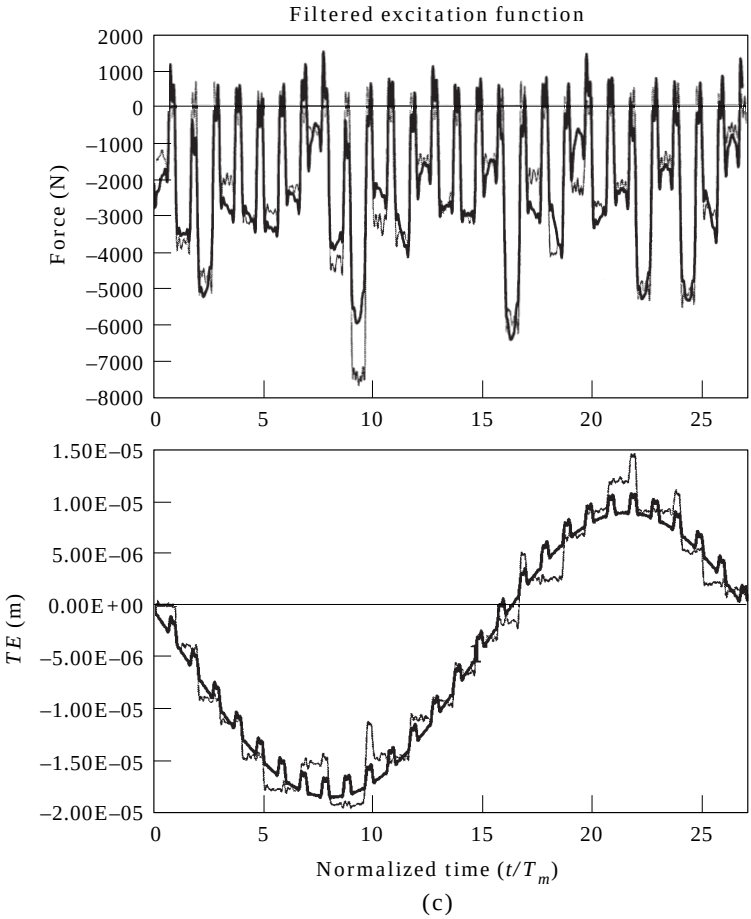

(c)

Fig. 16c.

Figure 16. Two different filtering levels on the excitation functions. (a) Original excitation functions and no-load TE; (b) filtered excitation spectra and no-load TE, —— level 1, ▲, level 2; (c) recomposition of the excitation functions (original functions are in Figure 16(a)), key as (b).

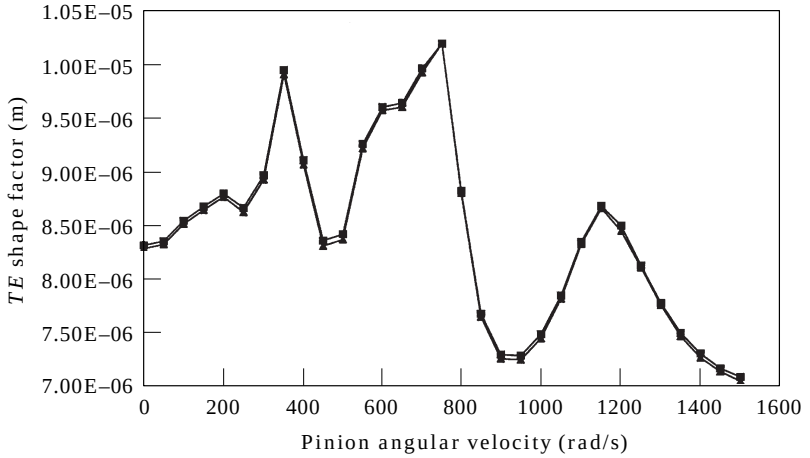

Figure 17. Influence of the filter on dynamic transmission errors. Key as Figure 16(b).

of recess) will be subsequently used as an indicator of the contact condition quality with respect to the ideal situation (full contact).

For a multi-mesh system with intermediate gears simultaneously in contact with two other pinions or gears (see Figure 6), the excitation functions associated to each mesh are not independent because they are controlled by the power circulation and the corresponding relative orientations of the base planes. The method introduced by Velex and Flamand [16] for epicyclic drives is applied and illustrated in Figure 7 by an example of mesh stiffness functions for three different relative orientations of the base planes (double stage gear set).

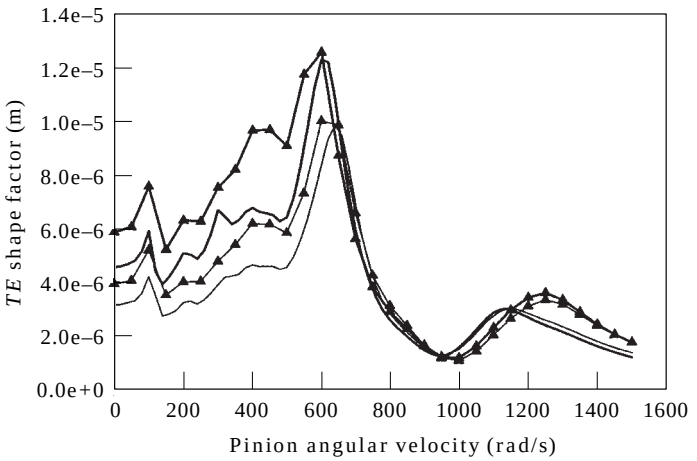

Figure 18. Influence of partial contact non-linearities on dynamic transmission errors. ℓ values (%): ——, 85, spectral; —▲—, 85, Newmark; ——, 68, spectral; —▲—, 68, Newmark.

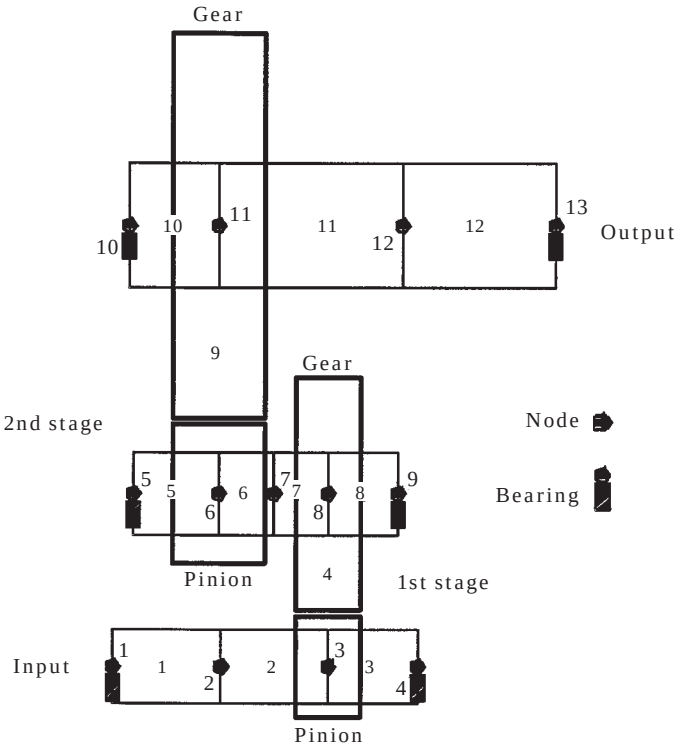

Figure 19. Finite element model of a double-stage unit (type A) (78 d.o.f.).

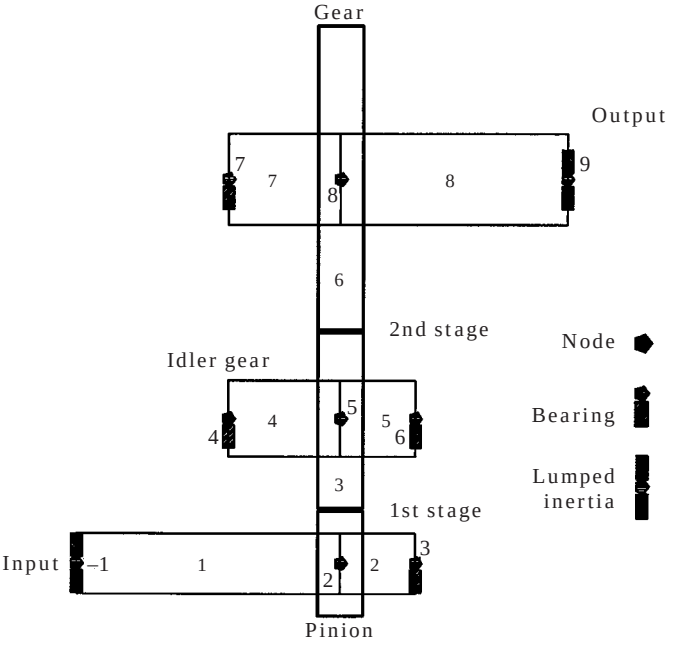

Figure 20. Finite element model of a double-stage unit (type B) (54 d.o.f.).

4. SOLUTION IN THE FREQUENCY DOMAIN

4.1. REDUCTION BY A RITZ METHOD

The principles of the methodology can be found in references [16, 29]. A particular stable solution of equation (14) is sought as a linear combination formed by the static solution $\bar{X}_o$ of equation (14) superimposed on a truncated linear

TABLE 3

Gear data

	1st stage		2nd stage	
	Pinion	Gear	Pinion	Gear
Number of teeth (Z_1, Z_2)	27	63	25	69
Width (mm)	72	72	100	100
Module (mm)	4		6	
Pressure angle (degree)	20		20	
Helix angle (degree)	0 (spur) or 16 (helical)		0 (spur) or 12 (helical)	
Addendum coefficient	1·0	1·0	1·0	1·0
Dedendum coefficient	1·4	1·4	1·4	1·4
Shift profile coefficient	0·0	0·0	0·0	0·0

TABLE 4

Shaft, bearing data

		Left side length (mm)	Right side length (mm)	External diameter (mm)
Input shaft		233·55	98·43	80·00
Intermediate shaft	1st stage	211·81	76·69	90·00
	2nd stage	92·43	196·07	90·00
Output shaft		96·77	366·70	133·35
Bearing		For all bearings, radial stiffness $k_p = 4 \times 10^8$ N/m		

TABLE 5

Gear data

	Pinion	Idler gear	Gear
Number of teeth (Z_1, Z_2)	23	39	67
Width (mm)	60	60	60
Module (mm)		6	
Pressure angle (degree)		20	
Helix angle (degree)		0 (spur) or 12 (helical)	
Addendum coefficient	1·0	1·0	1·0
Dedendum coefficient	1·4	1·4	1·4
Shift profile coefficient	0·0	0·0	0·0

TABLE 6

Shaft, bearing and load machine data

	Left side length (mm)	Right side length (mm)	External diameter (mm)
Input shaft	350·00	100·00	80·00
Intermediate shaft	150·00	100·00	100·00
Output shaft	150·00	300·00	120·00
Bearing	For all bearings, radial stiffness $k_p = 4 \times 10^8$ N/m		
Load and motor inertia	$I_m = 6$ kg m^2, $I_f = 6$ kg m^2		

combination of modeshapes [Φ] of the linear time-averaged system (pseudo-mode shapes): i.e.,

$$X = \bar{X}_o + [\Phi]\delta, \tag{21}$$

with δ the reduced unknown vector in the pseudo-modal basis.

Introducing $\bar{X}_o$ is interesting not only because parametric excitations depend on it, but also for the simulation of real geared drives often linked to the load machines by elastic couplings which can dynamically isolate the gear from its environment. In such a case, a solution constructed upon a modal basis only may be incompatible with a continuous torque transmission from the input to the output.

The present paper is mainly focussed on tooth contact dynamic analyses and the mode shapes in [Φ] are selected according to their percentages of strain energy stored in the gear elements [15, 16]. Upon rewriting strain and kinetic energies with

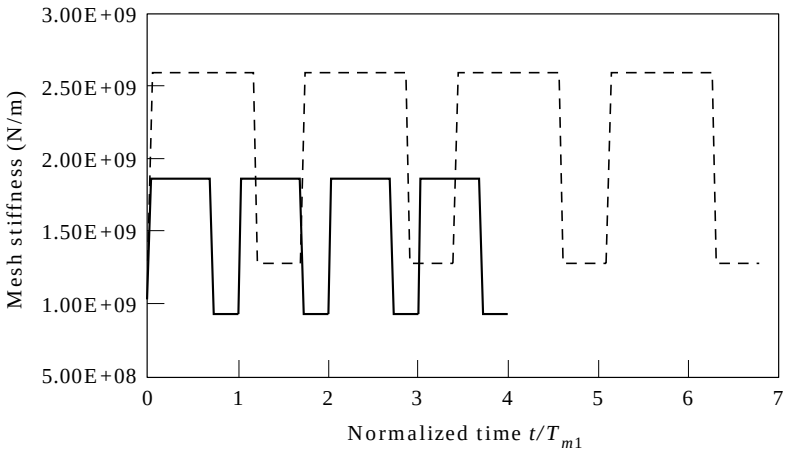

Figure 21. Mesh stiffnesses of the type A double-stage unit. ——, 1st stage; —, 2nd stage.

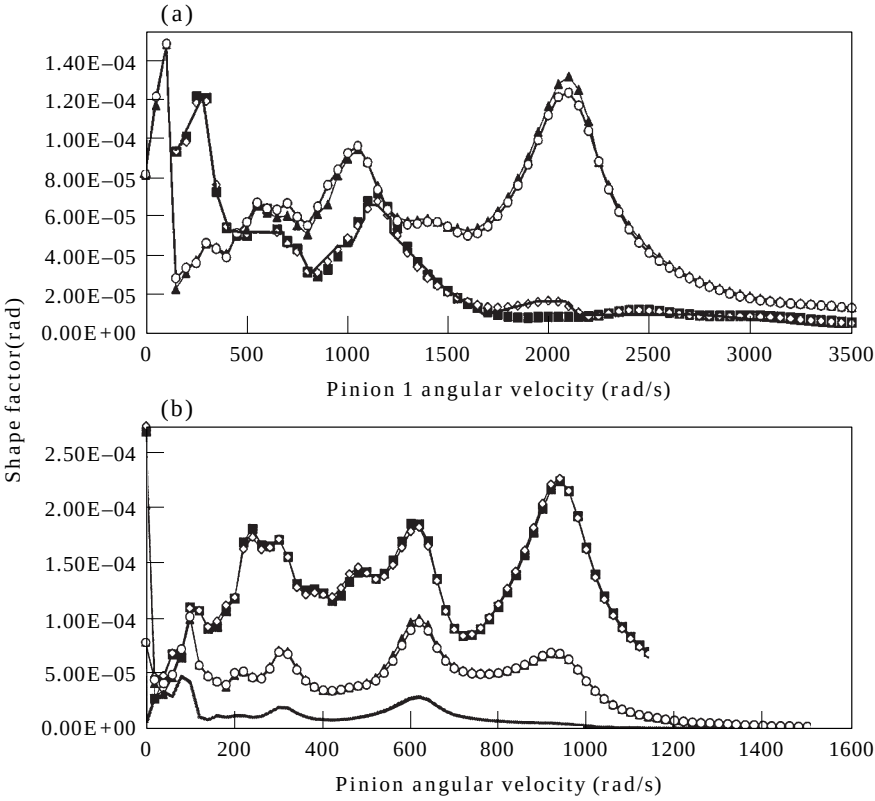

Figure 22. (a) Comparisons between the direct and spectral methods, type A multi-mesh system; (b) comparisons between direct and spectral methods, type B multi-mesh system. (a) —■—, pinion 1, spectral; —◇—, pinion 1, Newmark; —▲—, pinion 2, spectral; —○—, pinion 2, Newmark. (b) —■—, pinion, spectral; —◇—, pinion, Newmark; —▲—, intermediate gear, spectral; —○—, intermediate gear, Newmark; ——, output gear, spectral; ——, output gear, Newmark.

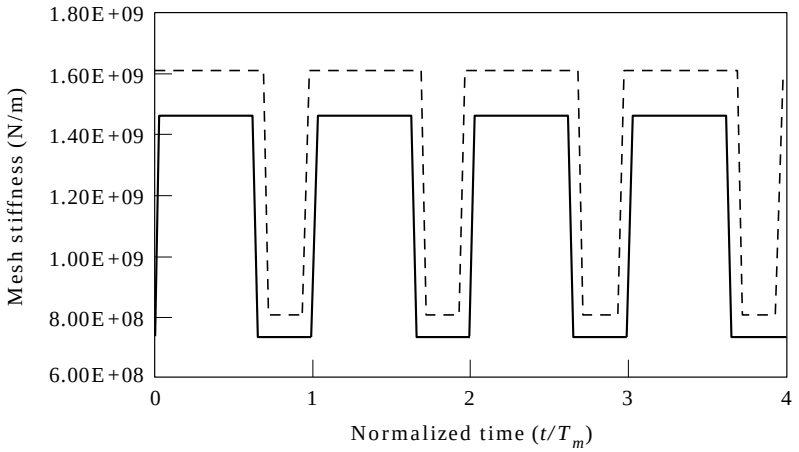

Figure 23. Mesh stiffnesses of the type B double-stage unit. ——, 1st stage; —, 2nd stage.

equation (21), Lagrange's equations together with the static equilibrium equation lead to the reduced differential system

$$[M_\phi]\ddot{\delta} + [C_\phi]\dot{\delta} + [K_\phi]\delta + \sum_{s}^{Nstage} \Delta k_s(t)[G_{\phi s}]\delta$$

$$= \sum_{s}^{Nstage} [-(\Delta k_s(t)^{\mathrm{T}}[\Phi][G_s]\bar{X}_o) + {}^{\mathrm{T}}[\Phi]\hat{H}_s(t)$$

$$+ \sum_{i}^{Ns(t)} k_{si}\delta e_s(M_i)\mathrm{H}(\Delta_{so}(M_i))^{\mathrm{T}}[\Phi]\hat{V}_{ms})], \tag{22}$$

with $[G_{\phi s}] = {}^{\mathrm{T}}[\Phi][G_s][\Phi]$.

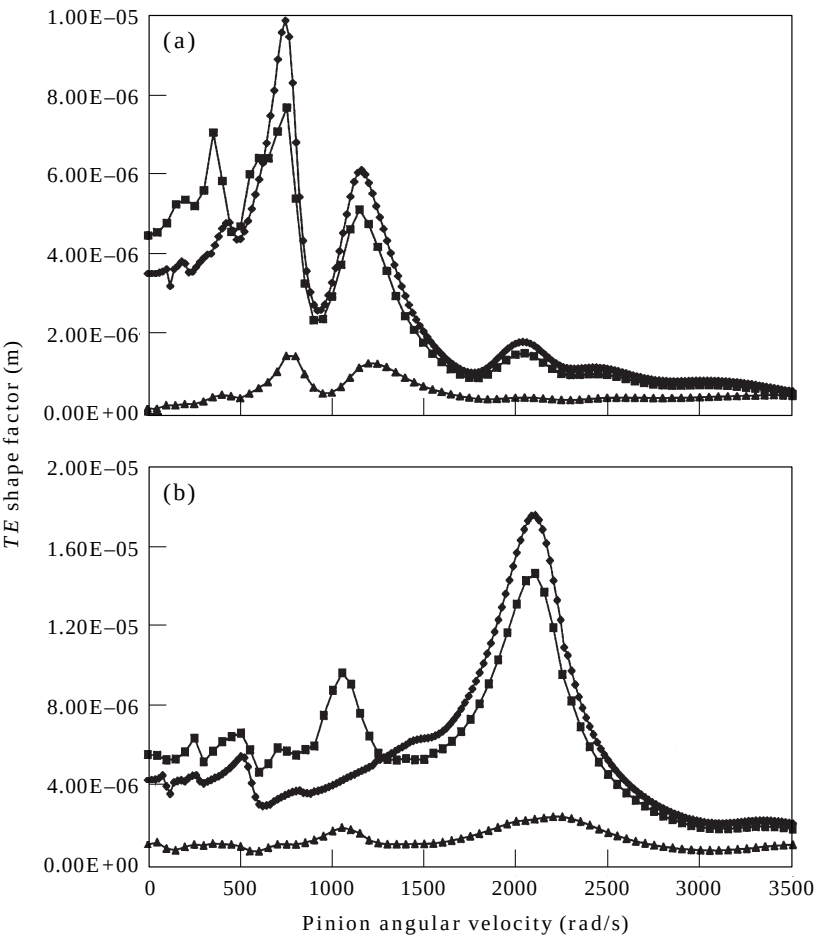

Figure 24. Influence of some profile modifications on dynamic transmission errors (double stage, type A, 25 mode shapes). (a) 1st stage; (b) 2nd stage. —■—, No modification; —◆—, short relief; —▲—, "optimum" relief.

TABLE 7

Major tooth critical frequencies for spur (helical) gears (type A)

Frequency (Hz)	ρ_1 (%)	ρ_2 (%)
3310 (3272)	41 (42)	1 ($\approx$0)
5009 (4831)	26 (17)	$\approx$0 ($\approx$0)
5443 (5492)	11 (15)	$\approx$0 (2·8)
1981 (1980)	6 (6)	$\approx$0 ($\approx$0)
3526 (3611)	1 ($\approx$0)	67 (69)

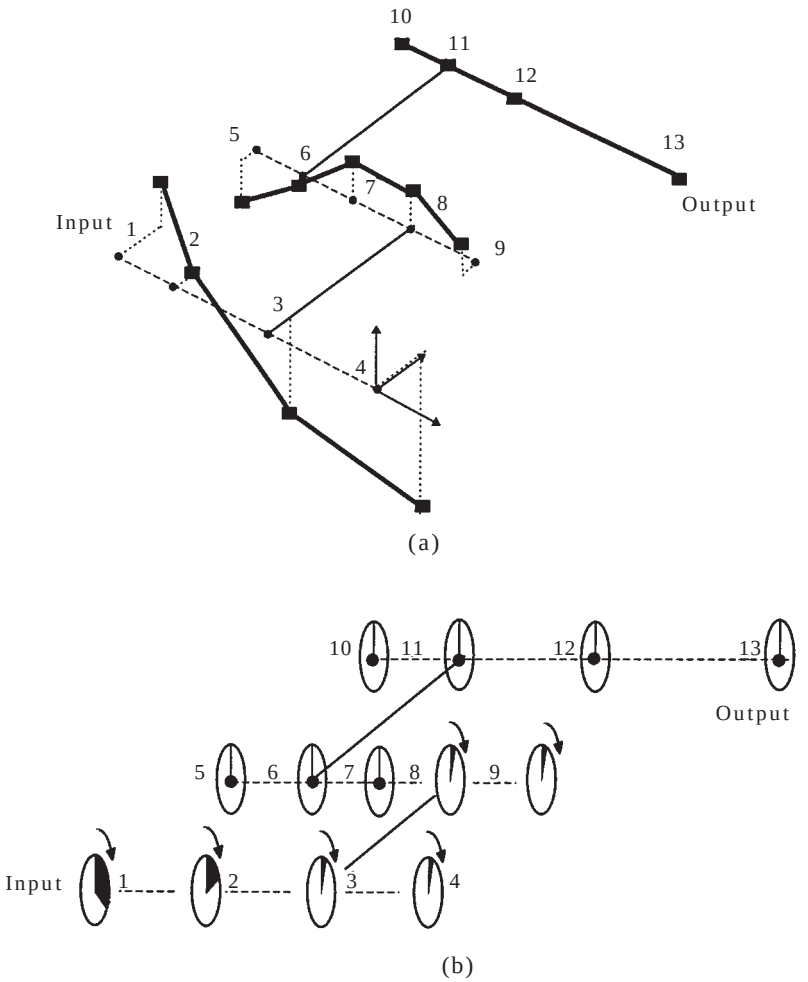

Figure 25. Modeshape at 3310 Hz (major tooth critical frequency for stage 1; spur gears, type A). (a) Bending; (b) torsion.

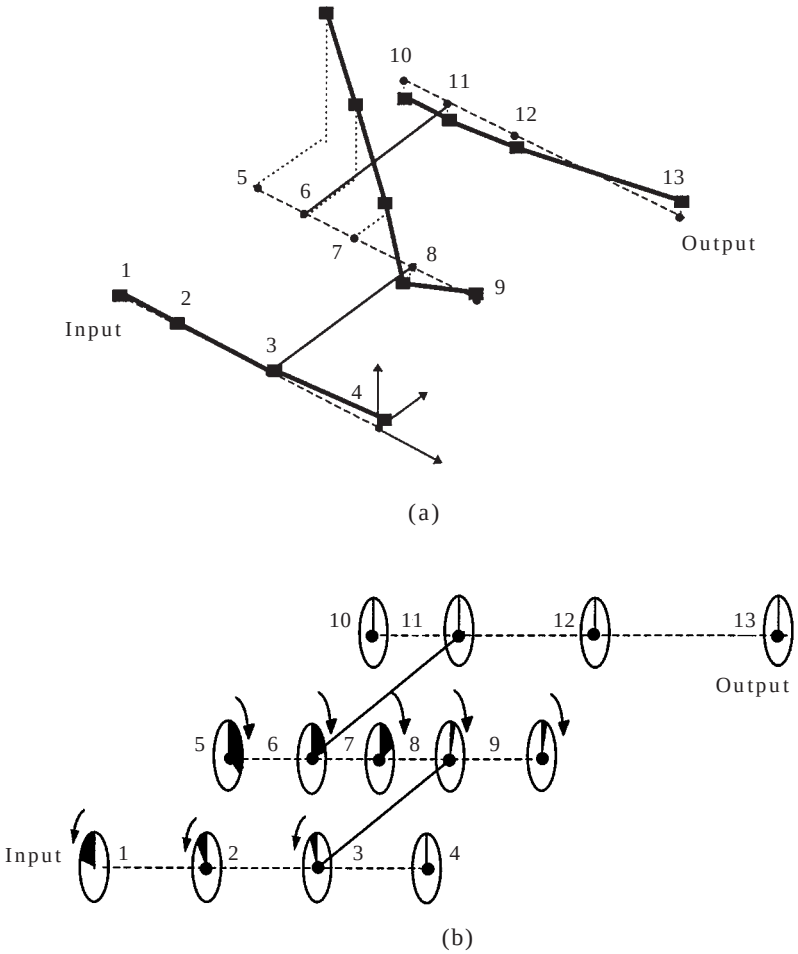

Figure 26. Modeshape at 3526 Hz (major tooth critical frequency for stage 2; spur gears, type A). (a) Bending; (b) torsion.

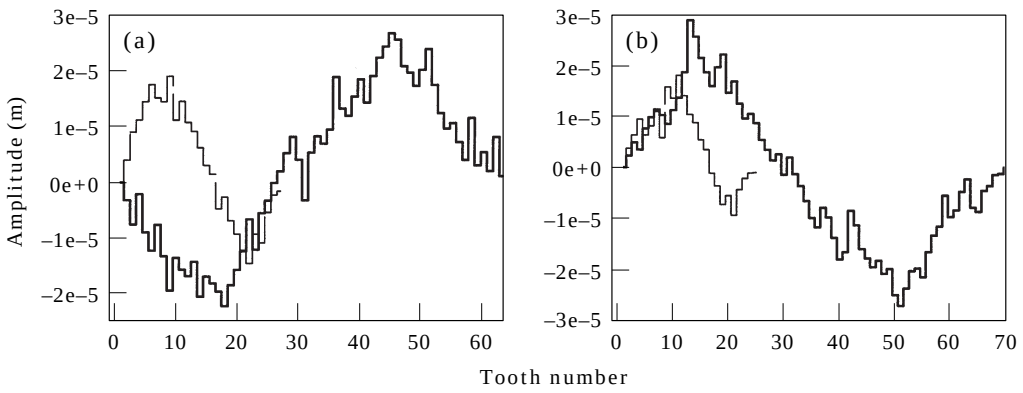

Figure 27. Pitch errors on the type A gear set. (a) Stage 1; (b) Stage 2. —, pinion; ——, gear.

As an illustration of the potential of the method in gear dynamics, the original equations of motion in the physical space (14) and the reduced system (22) are integrated by the same time-step Newmark procedure. The practical applications correspond to the single stage unit defined in Figure 8 and Tables 1 and 2. Figure 9 shows, for different modal bases $[\Phi]$, the corresponding maximum relative deviations in terms of dynamic transmission errors under load (results from equation (14) being the reference) which, for 25 modes, is reduced to less than 2% over the 0–1600 rad/s speed range.

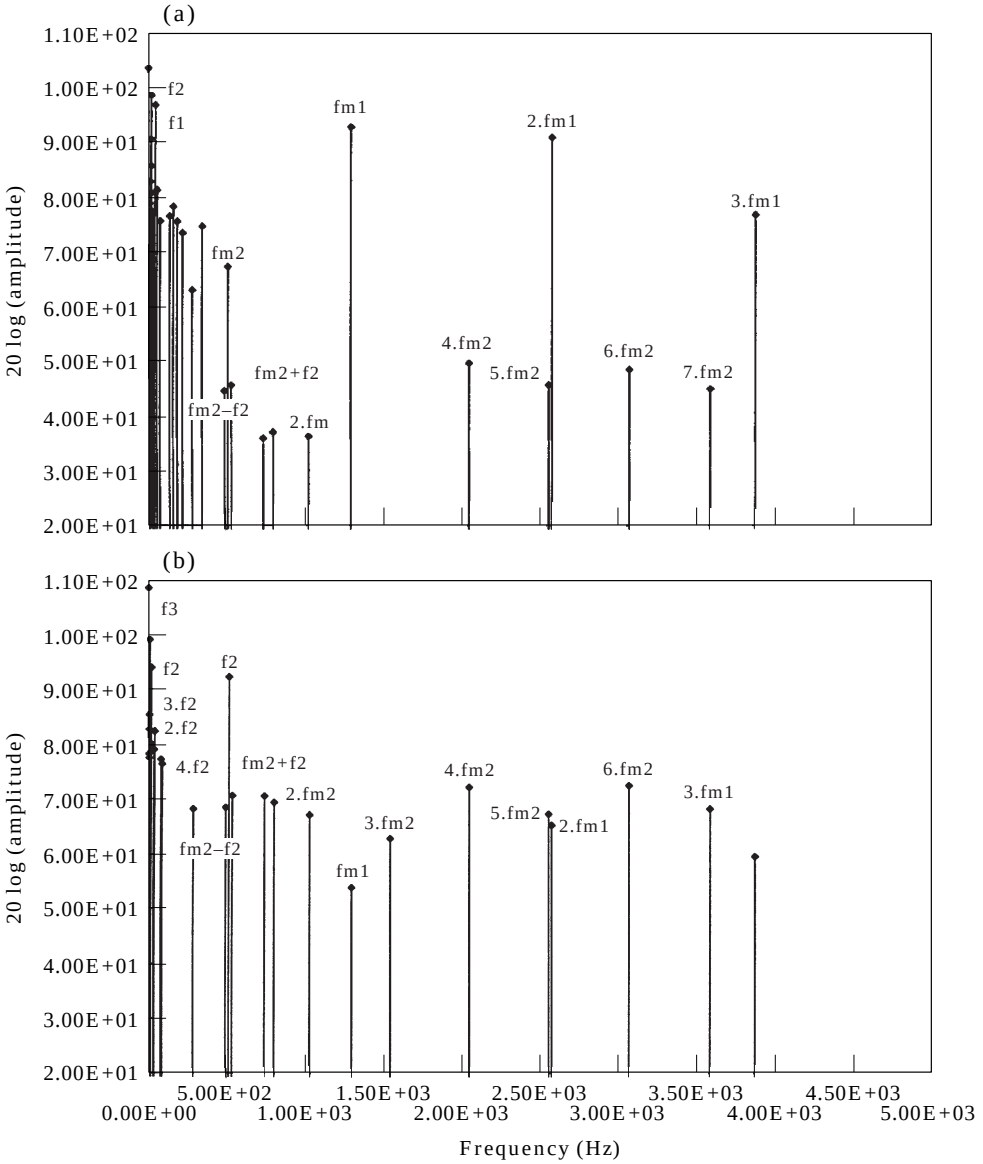

Fig. 28a & b.

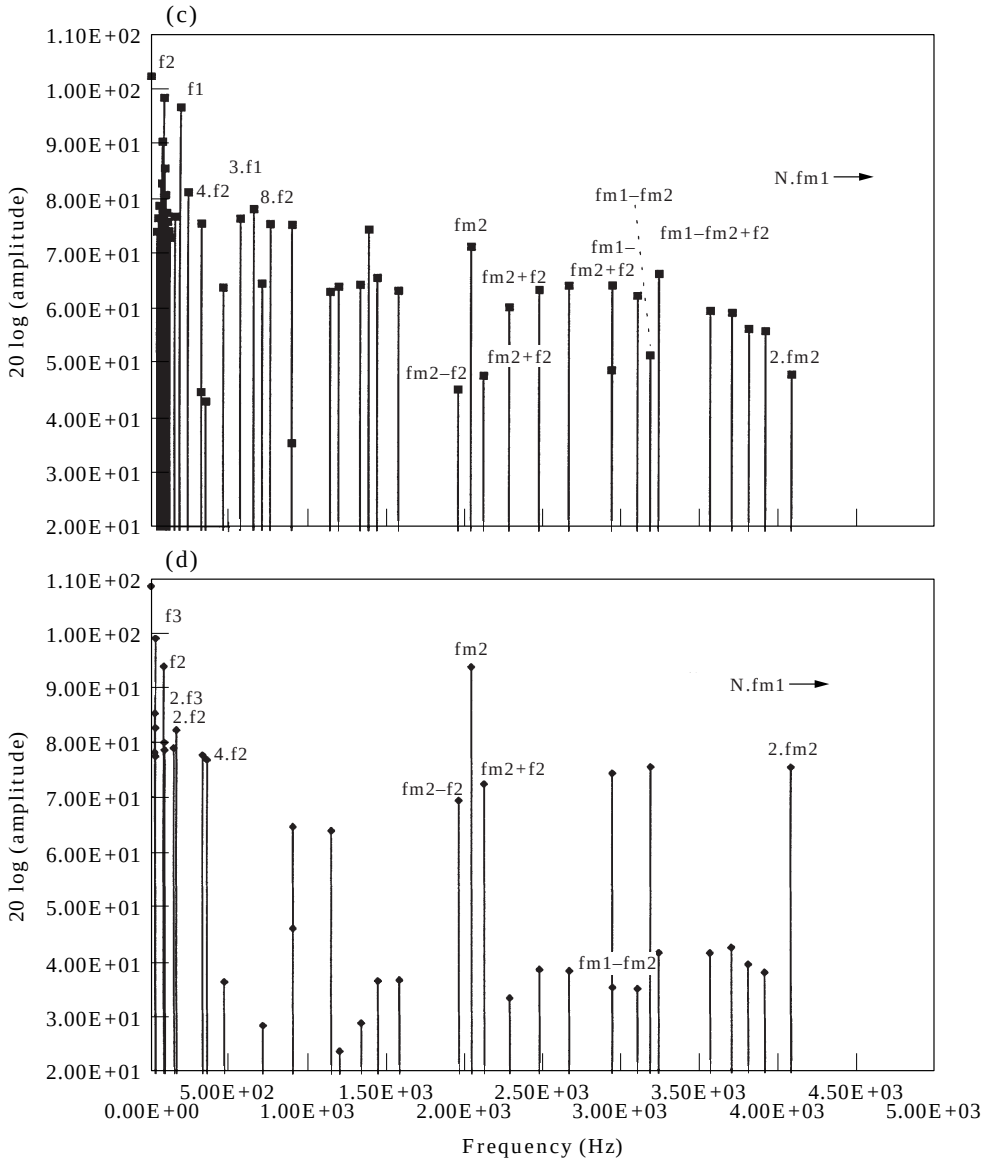

Fig. 28c & d.

Figure 28. (a) First stage transmission error spectrum at 300 rad/s on pinion 1, type A multi-mesh system; (b) second stage transmission error spectrum at 300 rad/s on pinion 1, type A multi-mesh system; (c) first stage transmission error spectrum at 1200 rad/s on pinion 1, type A multi-mesh system; (d) second stage transmission error spectrum at 1200 rad/s on pinion 1, type A multi-mesh system.

In equation (22), the modal mass and stiffness matrices $[M_\phi]$, $[K_\phi]$ are diagonal, the modal damping matrix $[C_\phi]$ is supposed to be diagonal according to Basile's hypothesis for moderate modal densities so that the αth equation can be expressed as

TABLE 8

Major tooth critical frequencies for spur (helical) gears (type B)

Frequency (Hz)	ρ_1 (%)	ρ_2 (%)
3557 (3522)	78 (78)	5 (5)
6248 (6222)	4 (4)	≈ 0 (≈ 0)
4488 (4440)	3·8 (2·8)	1·4 (2·7)
2338 (2342)	3·3 (3)	85 (81)
2768 (2750)	3 (2·7)	0·4 (≈ 0)

$$m_\alpha \ddot{\delta}_\alpha + c_\alpha \dot{\delta}_\alpha + k_\alpha \delta_\alpha = f_\alpha(t) - \sum_{s}^{Nstage} \Delta k_s(t) \langle [G_{\phi s}] \delta \rangle_\alpha, \tag{23}$$

where m_α, c_α, k_α are the αth diagonal terms of $[M_\phi]$, $[C_\phi]$ and $[K_\phi]$, respectively, while $f_\alpha(t)$ is the αth component of

$$\sum_{s}^{Nstage} ({}^{\mathrm{T}}[\Phi] \hat{H}_s(t) + \sum_{i}^{Ncs(t)} k_{si} \delta e_s(M_i) \mathrm{H}(\Delta_{so}(M_i))^{\mathrm{T}}[\Phi] \hat{V}_{ms} - \Delta k_s(t)^{\mathrm{T}}[\Phi][G_s] \bar{X}_o).$$

$\langle A \rangle_\alpha$ represents the αth component of vector A.

4.2. Fourier Transforms

Each equation (23) is projected in the frequency domain by using the classical Fourier Transform and becomes

$$D_\alpha(\omega) = T_\alpha(\omega) \left\{ F_\alpha(\omega) - \sum_{s}^{Nstage} \Delta K_s(\omega) \otimes \langle [G_\phi] D(\omega) \rangle_\alpha \right\}. \tag{24}$$

$\otimes$ denotes the product of convolution, $D_\alpha(\omega)$ is the αth component of $D(\omega) = \int_{-\infty}^{+\infty} \delta(t)\, \mathrm{e}^{\mathrm{j}\omega t}\, \mathrm{d}t$, and $T_\alpha(\omega) = \{(k_\alpha - \omega^2 m_\alpha) - \mathrm{j}\omega c_\alpha\} / \{(k_\alpha - \omega^2 m_\alpha)^2 + (\omega c_\alpha)^2\}$ is the transfer function associated with the αth modeshape of $[\Phi]$.

From a practical point of view, $F_\alpha(\omega)$, $\Delta K_s(\omega)$, Fourier Transforms of $f_\alpha(t)$ and $\Delta k_s(t)$, respectively, are some of the numerical results of the quasi-static analyses and are evaluated by using a classical discrete Fast Fourier Transform (FFT). This process implies the well-known constraint on signal samplings i.e., 2^N points of discretization whose consequences on the precision of the numerical solution are analyzed in section 5.2. In order to account for the speed reduction between two stages, the discretized excitation functions generated by each mesh are frequency scaled by using the system basic frequency as a common reference to all signals.

4.3. ITERATIVE SPECTRAL METHOD

Following Perret-Liaudet and Sabot [23], and Perret-Liaudet [24], the solutions of equations (24) are derived by an iterative procedure (Fixed-Point Method). Compared to that in references [23, 24], a relaxation of the solution has been introduced in order to improve the convergence. The numerical scheme can be synthesized as follows:

Initialization,

$$D_{\alpha}^{(\omega)}(\omega) = T_{\alpha}(\omega)F_{\alpha}(\omega); \tag{25}$$

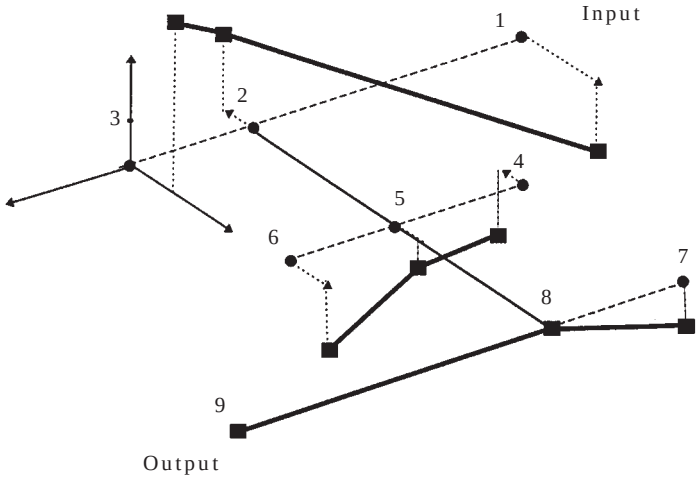

(a)

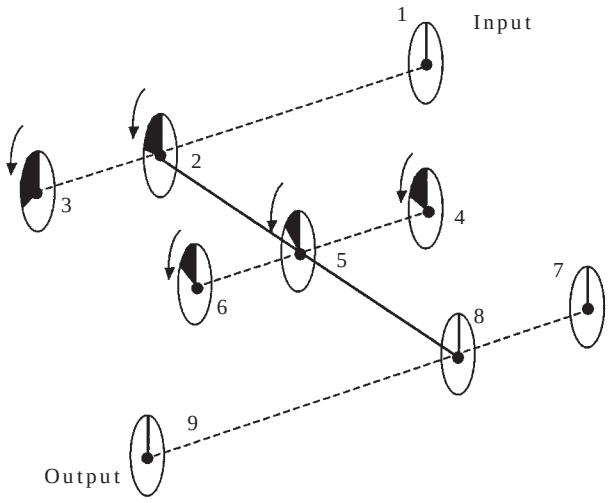

(b)

Figure 29. Modeshape at 3557 Hz (major tooth critical frequency for stage 1; spur gears, type B). (a) Bending; (b) torsion.

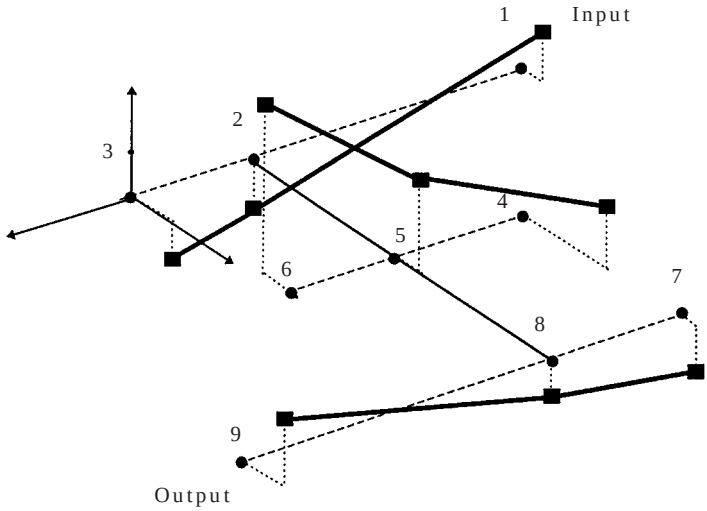

(a)

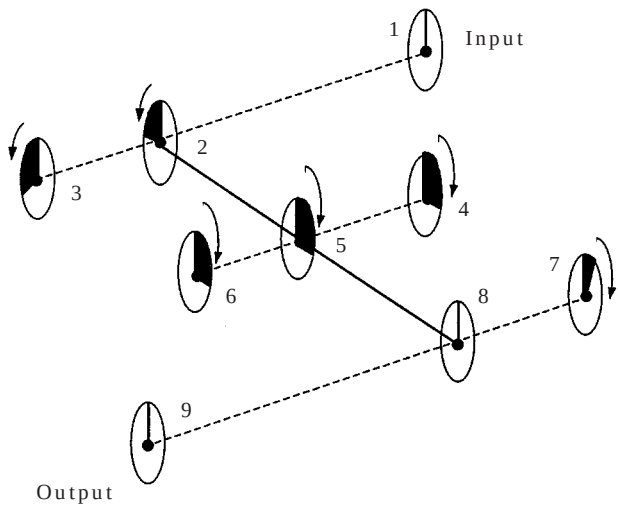

(b)

Figure 30. Modeshape at 2338 Hz (major tooth critical frequency for stage 2; spur gears, type B). (a) Bending; (b) torsion.

iteration L,

$$D_\alpha^{(L)}(\omega) = T_\alpha(\omega)\left\{F_\alpha(\omega) - \sum_s^{Nstage} \Delta K_s(\omega) \otimes \langle [G_\phi] D^{(L-1)}(\omega) \rangle_\alpha \right\}, \tag{26}$$

$$D_\alpha^{(L)}(\omega) \Leftarrow (1-\sigma) D_\alpha^{(L)}(\omega) + \sigma D_\alpha^{(L-1)}(\omega), \qquad 0 \prec \sigma \prec 0{\cdot}5. \tag{27, 28}$$

Convergence is evaluated by determining

$$R_\alpha = (ED_\alpha^{(L)} - ED_\alpha^{(L-1)})/ED_\alpha^{(L-1)}, \tag{29}$$

where $ED_{\alpha}^{(L)} = \int_{-\infty}^{+\infty} D_{\alpha}^{(L)}(\omega)^2 \, d\omega$; the iterative process is stopped when the maximum value of R_{α} is less than a given threshold $\varepsilon \prec\prec 1$.

A general discussion of the iterative scheme convergence in connection with the possible parametric instabilities caused by time-varying stiffnesses is difficult and beyond the scope of the present paper. Nonetheless, from a practical point of view, the following points have been observed.

(i) For the majority of the helical gear applications, convergence is good and relaxation is, most of the time, useless.

(ii) Problems may arise for spur gears (oscillating remainder R_{α}, for instance). According to the authors' experience, a relaxation factor $\sigma = 0{\cdot}2$ is generally sufficient to lead to a smooth convergence. However, divergence may happen especially for low number of d.o.f. models for which time-varying stiffnesses become prominent (particularly for purely torsional models).

(iii) As already reported [23], it seems that the positions of the divergence zones (if any) can be related to the parametric instability areas of the associated undamped free system.

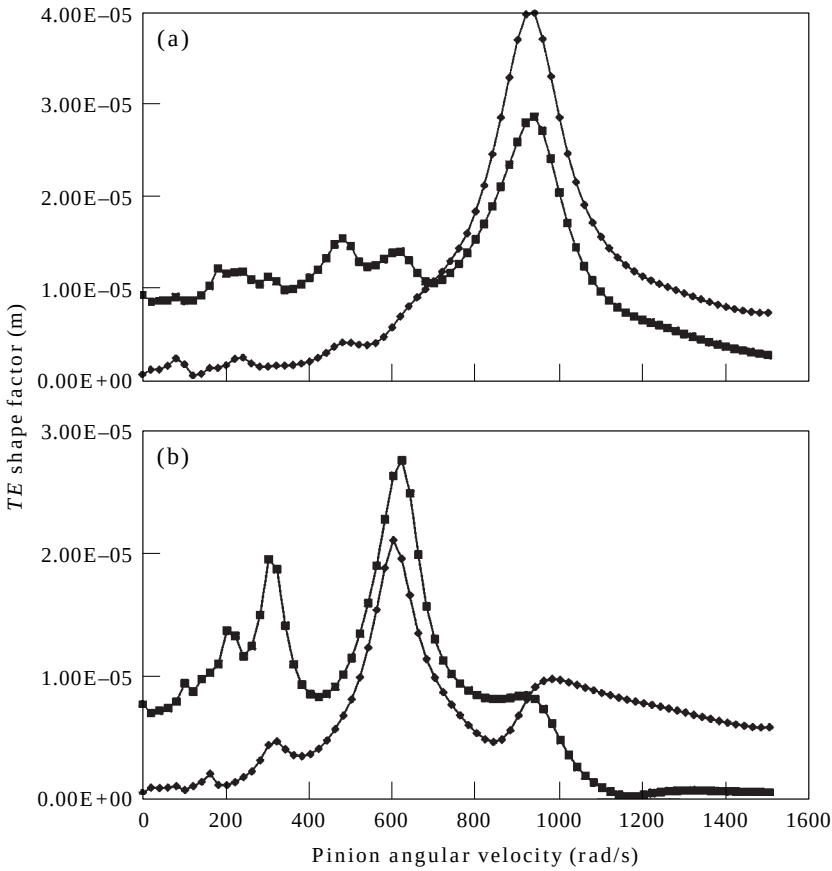

Figure 31. Dynamic transmission errors on the two stages. Influence of long reliefs '('optimum'' relief from a stage-by-stage analysis, 25 modeshapes). (a) 1st stage; (b) 2nd stage. —■—, No modification; —◆—, ''optimum'' relief.

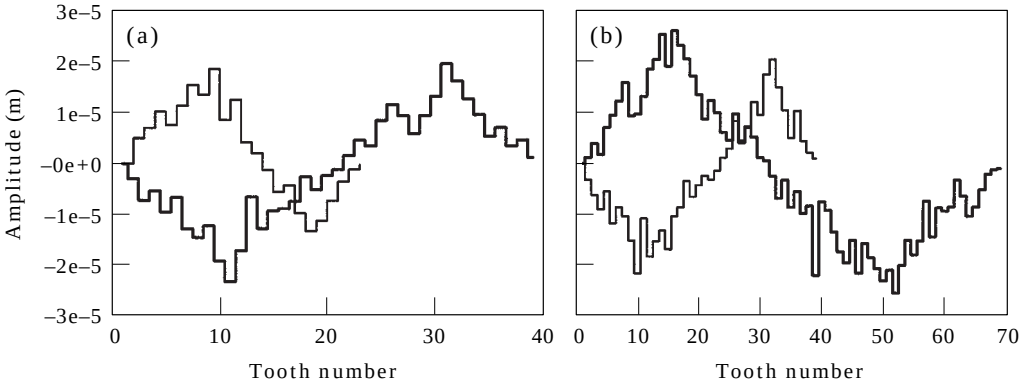

Figure 32. Pitch error distributions on the two meshes (type B drive). (a) 1st stage; (b) 2nd stage. (a) ——, pinion; ——, idler gear. (b) ——, Idler gear; ——, wheel.

Some technical modifications have been brought to the original technique proposed in references [23, 24]. The original discrete excitation spectra exhibit a series of equally spaced components whose number is equal to half of the number of points representing the original digitized signals (by virtue of the symmetry and skew-symmetry of the real and imaginary parts of the spectrum). In such conditions, it is not really advantageous to solve the state equations in the frequency domain since the number of operations in both time and frequency domains are comparable. Consequently, a filter is applied to the initial excitation spectra and also at each iteration in order to keep the relevant frequency components only and limit the expansion of the spectrum bandwidths generated by the successive products of convolution (see equation (26)). Two criteria are simultaneously considered: i.e., (i) the contribution of each frequency component to the total signal energy which is evaluated by calculating $E_\alpha(\omega) = |D_\alpha(\omega)|^2 / \int_{-\infty}^{+\infty} |D_\alpha(\omega)|^2 \, d\omega$ (the threshold used in the numerical applications is 1%); (ii) the significant width of the spectra, upon assuming that contributions at a frequency higher than $f_{\max i} = n_f \max(f_{mesh})$ for $n_f = 10$, can be neglected in mechanical vibration analysis.

Another modification of the original procedure is the calculation of the product of convolution in the frequency domain in order to avoid time-consuming transfers between the frequency and time domains until the final solution is obtained. All excitation spectra being discrete, they can be expressed as a combination of impulses modelled by using the Dirac delta function δ as

$$\Delta K_s(\omega) = \sum_{nfk=1}^{n_k} \{\Re K_{nfk}(\delta(\omega + \omega_{nfk}) + \delta(\omega - \omega_{nfk})) + j\Im K_{nfk}(\delta(\omega + \omega_{nfk}) - \delta(\omega - \omega_{nfk}))\}, \tag{30}$$

$$\langle [G_\phi] D(\omega) \rangle_\alpha = \sum_{nfg=1}^{n_g} \{\Re G_{nfg}(\delta(\omega + \omega_{nfg}) + \delta(\omega - \omega_{nfg})) + j\Im G_{nfg}(\delta(\omega + \omega_{nfg}) - \delta(\omega - \omega_{nfg}))\}, \tag{31}$$

where $\Re K_{nfk}(\cdot)$, $\Im K_{nfk}(\cdot)$, $\Re G_{nfg}(\cdot)$ and $\Im G_{nfg}(\cdot)$ represent the real and imaginary parts of the discrete spectra of $\Delta K_s(\omega)$ and $\langle [G_\phi] D(\omega) \rangle_\alpha$, n_k and n_g are the numbers of relevant frequencies after filtering of $\Delta K_s(\omega)$ and $\langle [G_\phi] D(\omega) \rangle_\alpha$.

At each iteration, the different products of convolution are replaced by finite summations over a range of selected frequency components. Finally, upon using the relation $\delta(\omega - \omega_a) \otimes \delta(\omega - \omega_b) = \delta(\omega - (\omega_a + \omega_b))$, one obtains

$$\Delta K_s(\omega) \otimes \langle [G\phi] D(\omega) \rangle_\alpha$$

$$= \sum_{nfk}^{n_k} \sum_{nfg}^{n_g} [\Re K_{nfk} \Re G_{nfg} - \Im K_{nfk} \Im G_{nfg}][\delta(\omega - (\omega_{nfk} + \omega_{nfg})) + \delta(\omega + (\omega_{nfk} + \omega_{nfg})$$

$$+ \mathrm{j} \sum_{nfk}^{n_k} \sum_{nfg}^{n_g} [\Re K_{nfk} \Im G_{nfg} + \Im K_{nfk} \Re G_{nfg}][\delta(\omega + (\omega_{nfk} + \omega_{nfg}))$$

$$- \delta(\omega - (\omega_{nfk} + \omega_{nfg}))]$$

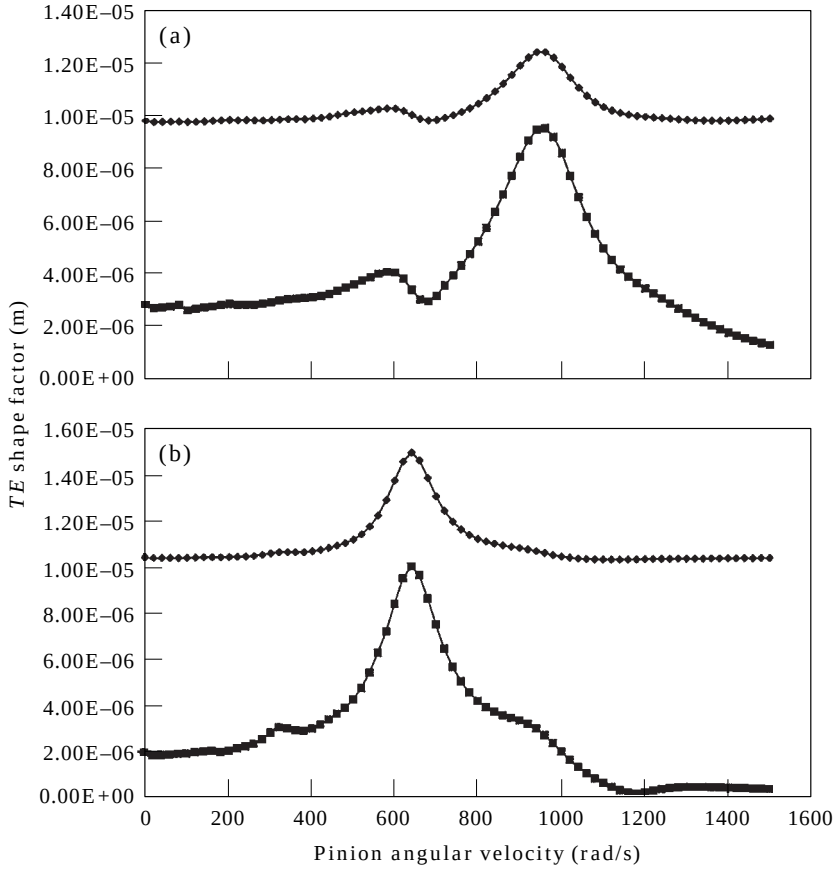

Figure 33. Influence of pitch errors on transmission errors (type B drive, 25 modeshapes). (a) 1st stage; (b) 2nd stage. —■—, No modification. —◆—, pitch errors.

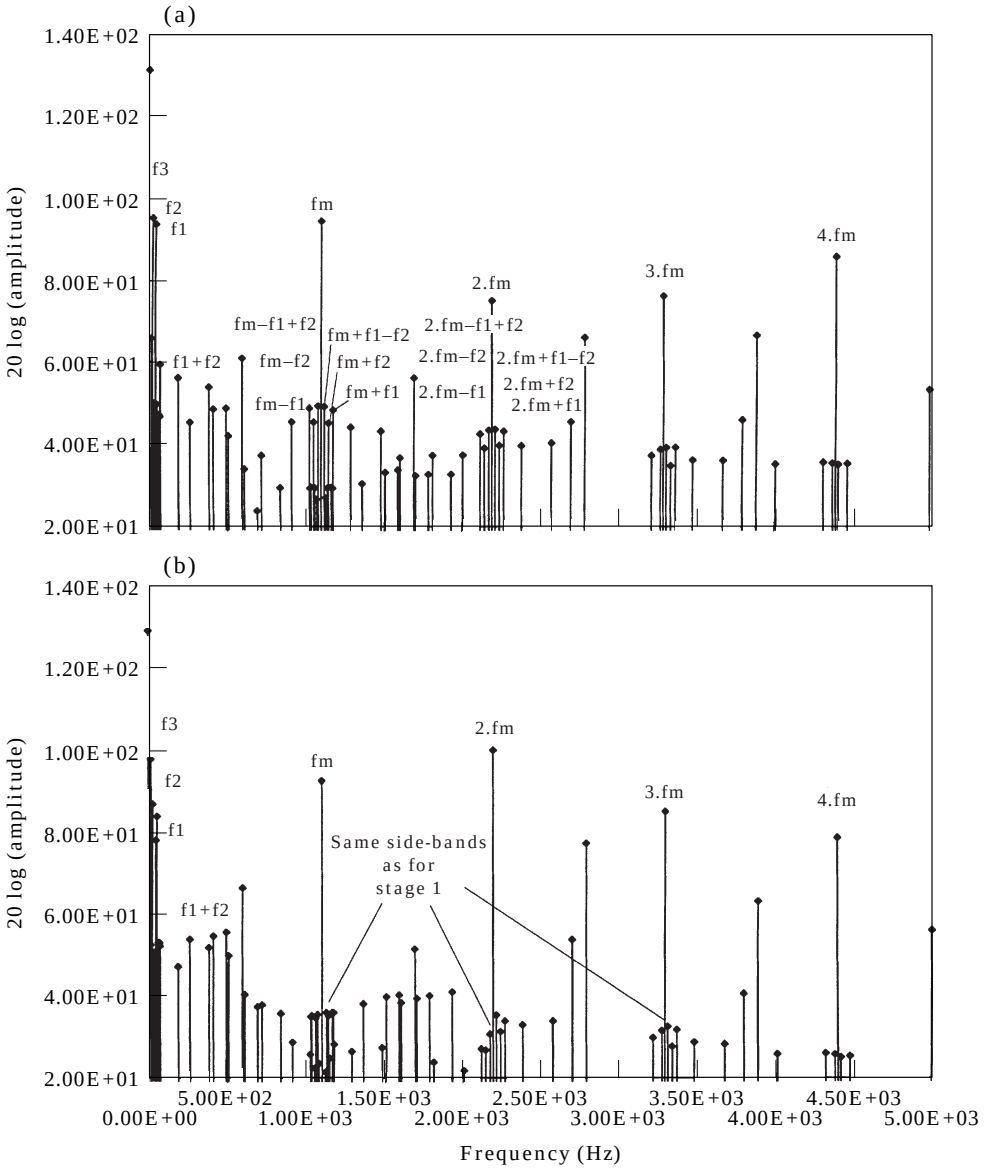

Fig. 34a & b.

$$+\sum_{nfk}^{n_k}\sum_{nfg}^{n_g}[\Re K_{nfk}\Re G_{nfg}+\Im K_{nfk}\Im G_{nfg}][\delta(\omega-(\omega_{nfk}-\omega_{nfg}))$$

$$+\delta(\omega+(\omega_{nfk}-\omega_{nfg}))]$$

$$+\mathrm{j}\sum_{nfk}^{n_k}\sum_{nfg}^{n_g}[-\Re K_{nfk}\Im G_{nfg}+\Im K_{nfk}\Re G_{nfg}][\delta(\omega+(\omega_{nfk}-\omega_{nfg}))$$

$$+\delta(\omega-(\omega_{nfk}-\omega_{nfg}))], \tag{32}$$

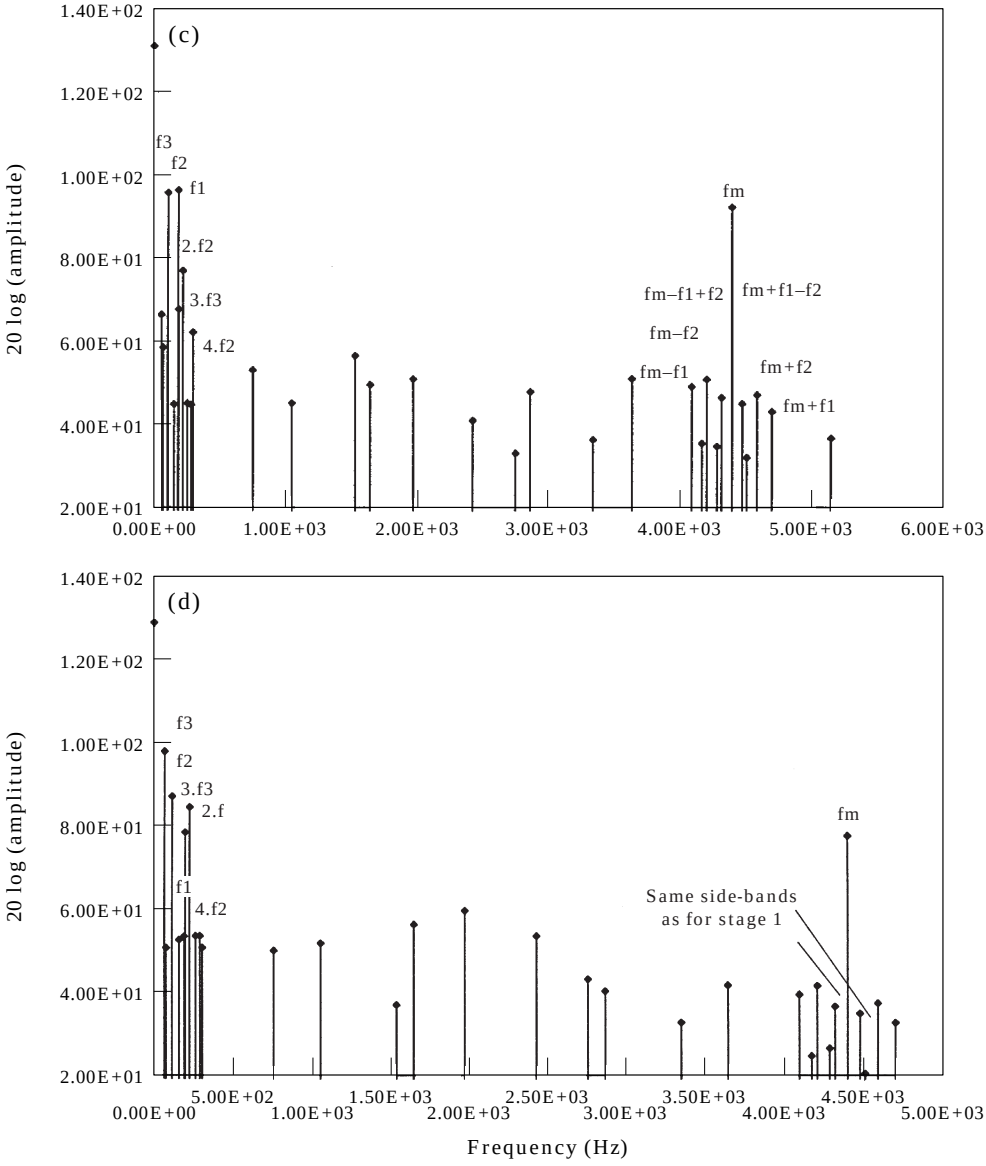

Fig. 34c & d.

Figure 34. (a) First stage transmission error spectrum at 300 rad/s on pinion 1, type B multi-mesh system; (b) second stage transmission error spectrum at 300 rad/s on pinion 1, type B multi-mesh system; (c) first stage transmission error spectrum at 1200 rad/s on pinion 1, type B multi-mesh system; (d) second stage transmission error spectrum at 1200 rad/s on pinion 1, type B multi-mesh system.

which can be rapidly calculated by numerical means. The operations are kept limited to the significant amplitudes and, at each iteration, only the relevant frequencies (dimensioned values—see section 4.2) and amplitudes are stored and used in the next iteration. It can be seen from the structure of equation (32) that

the frequencies corresponding to the harmonic combinations of each mesh do appear in the process.

5. ON THE NUMERICAL BEHAVIOUR OF THE SPECTRAL METHOD

5.1. COMPARISONS WITH TIME-STEP INTEGRATIONS ON A SINGLE MESH GEAR SET

In order to validate the proposed methodology, several response curves delivered by the iterative spectral method and a time-step integration (implicit Newmark's scheme) combined with a normal contact algorithm [22] are compared. The time-step procedure, considered as the reference in what follows, accounts for contact non-linearities and solves the original equations of motion without any of the simplifications of equations (15)–(20) which are inherent in the Spectral Method. For both methods, each mesh period is discretized into 64 time-steps. The single mesh system under consideration is depicted in Figure 8 and the gear-shaft-bearing data are listed in Tables 1 and 2. For all selected modeshapes (15 modes in this example), a unique damping factor of 0·1 is introduced in the simulations. This numerical value corresponds to the experimentally identified data of Kubo *et al*. [37] for spur gears. (A review of some significant measured damping factors for gear tooth critical frequencies can be found in reference [3]).

The first set of comparisons deals with ideal errorless spur and helical gears so that the only excitations come from the time-varying mesh stiffness. Transmission error shape factors $SF(TE)$ defined as

$$SF(TE) = \left[\sum_i \Re TE_i(\omega)^2 + \Im TE_i(\omega)^2 \right]^{1/2}, \tag{33}$$

with $\Re TE_i(\omega)$ and $\Im TE_i(\omega)$, the ith frequency component (real and imaginary parts, respectively) of transmission error, are evaluated and their evolutions versus pinion speed are plotted in Figure 10. A good agreement between the two methods is observed although some discrepancies are noticed at high speeds (near 1200 rad/s). They are attributed to the averaged structure vector in the spectral method whose influence, because of the bending slopes ϕ and Ψ, may be non-negligible when pinion and/or gear are not centred on their shafts. (It can be observed from equation (7) that the ϕ and Ψ components of the structure vector $V_s(M_i)$ are the only ones depending on the position of M_i and, consequently, on the averaging operation in equation (8).) With the usual damping levels in gear dynamics, the pseudo-modal truncation implies only a few tests and, generally, is not a problem. Further details on the selection of the relevant mode shapes for tooth critical frequency analysis on multi-mesh gear sets can be found in reference [16].

Multi-frequency excitations are introduced by (a) a time-varying mesh stiffness, (b) linear short profile reliefs on pinion and gear tooth tips (amplitude 30 μm, extent of modification 20% of the active profile), (c) pitch errors on the pinion only (in order to keep reasonable computational times for the time-step technique) whose distribution and amplitudes are given in Figure 11. An image of the excitation spectra is given by the frequency contents of the quasi-static

transmission error under load represented in Figure 12. Transmission error shape factor evolutions calculated by the two methods again compare favourably as shown in Figure 13. For this example, computational times are approximately five times (spur gears) and eight times (helical gears) shorter when using the iterative spectral method.

Finally, one of the limits of the iterative spectral method is pointed out on the spur gear example with a lower modal damping factor of 0·05 (see Figure 14). The response curve has been determined by time-step integrations for steady-state conditions and by keeping the same initial conditions at all speeds ($X = \bar{X}_o$, $\dot{X} = \ddot{X} = 0$) which make it impossible to determine any multiple solutions and related unstable branches. However, the gear dynamic behaviour is clearly dominated by a large amplitude jump at the major critical speed (softening behaviour corresponding to single-sided impacts) which, as obvious from the theoretical formulation, is not reproduced by the spectral method. Consequently, this method seems to be suitable for essentially heavily loaded gear systems. From a qualitative point of view, possible tooth separations could be detected during computation by examining the minimum value of each mesh deflection as backlash probably occurs at stage s if $\Delta_s(M_i) \leqslant 0$, for all points M_i of stage s.

5.2. INFLUENCE OF THE DISCRETIZATION AND OF THE FILTER

The initial excitation functions being introduced by using numerical Fast Fourier Transforms, one of the basic constraints comes from the total number of discretization steps which has to be compatible with the use of the classical FFT's algorithm, i.e., 2^N points (N integer) for most of the practical situations. Depending on the gear tooth numbers and on the gear set arrangement, 2^N points over one stage period can imply a non-integer number of discretization steps per mesh period which leads to an artificial modulation of the mesh frequency. A detailed analysis is presented in reference [27]; for modal damping factors between 0·05 and 0·1, it is found that dynamic response curves are not really modified by these numerical errors as illustrated in Figure 15 for an errorless spur gear example analyzed with 32, 18·963, 12 and 9·482 time-steps per mesh period.

For broad band excitation spectra, the practical interest of the proposed method mainly lies on the filtering of the excitation functions during the iterative process. The filter influence is analyzed by comparing the dynamic transmission errors obtained by using two different filtering levels (see Figures 16 and 17). A wide range of frequencies is conserved in level 1 while level 2 deals with the prominent frequency components only. It is clear from Figure 17, that, for the treated example, the use of rough excitation spectra (level 2) gives excellent results almost superimposed to the response curve calculated with more refined spectra. Computational times associated to levels 2 and 1 are in a 1 to 3 ratio.

5.3. INFLUENCE OF PARTIAL CONTACT LOSSES

In this section, a parametric analysis is conducted in order to determine the influence of some common mounting errors or defects on the Iterative Spectral Method precision. As already discussed, backlash cannot be reproduced but the

question of partial contacts together with the use of the linearized expressions of section 3.3 has still to be addressed. Partial contacts on tooth flanks are introduced through a pinion deviation (misalignment) and the difference in tooth contact quality with respect to the nominal case is estimated by the partial contact index ℓ defined in section 3.3. It is observed in Figure 18 that transmission errors compare favourably for $\ell = 85\%$ (15% of contact loss over one mesh period at low speed). For $\ell = 68\%$, the positions of the response curve peaks are still acceptable but the low-medium speed transmission errors calculated by ISM and time-step integrations become significantly different. The Iterative Spectral Method does not converge correctly for ℓ below 65%. From a physical point of view, dynamic response levels increase and major tooth critical frequencies are shifted towards lower speeds with an increasing misalignment amplitude. It is to be noted that simulations with larger pseudo-modal bases (20 and 40 modes) lead to similar response curves.

5.4. COMPARISONS WITH TIME-STEP INTEGRATIONS—DUAL MESH GEAR SETS

Comparisons are extended to two classical gear arrangements, i.e., dual mesh drives with four gears referred to as type A systems and dual mesh drives with three gears (type B). The corresponding finite element models are described in Figures 19 and 20, gear, shaft data are given in Tables 3–6. Pinions and gears are supposed to be perfect and the only excitations come from the time-varying mesh stiffnesses. In this section, only spur gear sets are considered.

The three shaft axes of the type A system in Figure 19 lie in the same plane and the arbitrary initial phasing between the two mesh stiffness functions is set to be zero as illustrated in Figure 21. All radial bearing stiffnesses are equal to $4E8$N/m, the input torque is 1500 Nm and a unique modal damping factor of 0·1 is introduced. Computations in time-domain are conducted by the Newmark scheme and shape factors are evaluated over the complete system period. The shape factors of the pinion torsional degree of freedom obtained by time-step integrations and by the spectral method are plotted in Figure 22(a). A very good agreement is observed even if some slight differences appear near the major tooth critical speed of stage 2.

Similar comparisons are made with the type B dual mesh example (see Figure 20); the shaft axes are again in the same plane and the resulting phasing between the two mesh stiffnesses is imposed by the power circulation (see Figure 23). The response curves delivered by the time-step scheme and the spectral method (see Figure 22(b)) are extremely close and prove the validity of the proposed methodology.

From a physical point of view, there are no clear couplings between the two meshes of the type A system. On the contrary, similar critical speeds are found for stages 1 and 2 of the type B gear set. A more detailed discussion of the response spectral contents and mesh dynamic couplings is deferred to section 6.

6. SOME APPLICATIONS TO DOUBLE MESH GEAR SETS

The potential of the proposed iterative spectral method is illustrated by some applications to conventional fixed-axis systems with spur and helical gears. The models account for time-varying mesh stiffnesses, flexible shafts, bearings, and multi-frequency excitations generated by profile modifications and/or pitch errors.

6.1. TYPE A: TWO MESHES, FOUR GEARS

The mechanical system is the same as the one defined in section 5.4. Two different kinds of profile modifications (identical on both meshes) are introduced: (i) linear short reliefs of 30 μm amplitude on pinion and gear tooth tips with an extent of modification corresponding to 20% of the active profile length; (ii) linear long profile reliefs whose extents of modification are 40% of the active profile.

Dynamic transmission error shape factors for each mesh are given in Figure 24, no clear couplings between the two stage dynamic behaviours are observed. The most significant percentages of modal strain energy stored in mesh one (ρ_1) and in mesh two (ρ_2) for spur and helical gears in Table 7 reveal that the two meshes are largely uncoupled and that tooth critical frequencies for spur and helical gears are nearly identical. The mode shapes corresponding to the two major tooth critical frequencies for mesh one (3310 Hz) and two (3526 Hz) are represented in Figures 25 and 26. The independence of the two meshes for bending and torsional vibrations is clearly confirmed for these two modes. Because of the speed reduction, critical frequency coincidences on the second stage are at higher speeds compared to stage one.

As already reported for spur gear single mesh systems [29, 30, 31], long reliefs can largely reduce the vibration levels over the whole speed range for a given load while short reliefs are far less effective in reducing transmission error variations.

For the spur gear set with no profile modification, the pitch error distributions in Figure 27 are introduced in order to analyze the transmission error spectral contents after filtering. It is clear that a precise identification of every spectral ray is not simple because of the many possible harmonic combinations, consequently, only the clearly identified components are commented in the following discussion. For clarity, the spectrum representations are limited to 5 kHz although higher frequencies are conserved along the iterative process and in the final results.

(a) *Medium speed spectra* (300 rad/s)

The input stage TE spectrum in Figure 28(a) is mostly dominated by the input and intermediate shaft rotational frequencies (f_1, f_2), by its mesh frequencies (Nfm_1, N integer). The second stage mesh frequency and its multiples (Nfm_2) are also present but with lower amplitudes.

The output stage (see Figure 28(b)) exhibits some significant rays at the intermediate and output shaft frequencies (f_2, f_3), at mesh frequencies (Nfm_1, Nfm_2). Only some modulation side-bands between fm_2 and f_2 are observed, the relative importance of f_2 which is the only common frequency of the two stages is pointed out.

(b) *High speed spectra* (1200 rad/s)

More frequencies are conserved by the filter (see Figures 28(c) and (d)) with, in addition to what is reported in (a), some significant harmonic combinations between the mesh frequencies ($fm_1 - fm_2$), the mesh frequencies and the intermediate shaft rotation ($fm_1 - fm_2 \pm f_2$). The amplitudes at Nfm_2 are larger and some higher harmonics of f_1, f_2 and f_3 are involved.

(c) *General comments*

The f_3 component is generally weak because of the speed reduction effect and, in agreement with the preceding remarks on mesh dynamic couplings, there is no evidence of strong direct interactions between the input and output shaft rotational frequencies. Low frequency contents of transmission errors are particularly rich with some strong modulations between f_1, f_2, f_3 and each stage basic frequency. As opposed to the single stage example (Figure 12), no modulation side-bands of the form $Nfm_1 \pm Mf_1$ appear in the filtered spectra of this double stage application.

6.2. TYPE B: TWO MESHES, THREE GEARS

The model under consideration is depicted in Figure 20, and gear and shaft geometries are defined in Tables 5 and 6. As in section 6.1, modal strain energy distributions are evaluated (Table 8) and the two mode shapes associated with the major tooth critical frequencies (with the largest percentages of modal strain energy) are shown in Figures 29 and 30. As opposed to the previous dual mesh drive, some couplings between stages 1 and 2 emerge.

For long profile reliefs on both stages (same definition as in section 6.1), the corresponding spur gear transmission error curves are plotted in Figure 31. Transmission error shape factors are reduced at low and medium speeds but, contrary to what is observed on the type A example, long reliefs are rather ineffective near the major critical speeds. This difference is caused by the stronger interactions (compared to type A) between the two meshes and it seems that optimizing spur gear profile modifications on a stage-by-stage basis may be inadequate.

The next example deals with pitch errors introduced on every gear of the reduction unit, their amplitudes and distributions are shown in Figure 32. Transmission errors are determined for helical gears ($\beta = 12^\circ$) and their evolutions versus the first stage pinion speed are represented in Figure 33. As already reported for single mesh systems [22], pitch errors increase the average transmission error levels but do not introduce any additional critical tooth frequencies. On the other hand, amplifications at major critical speeds (with respect to quasi-static transmission error levels) are lower than for errorless gears. As for the errorless gear set, the major critical tooth frequency of one given mesh can be observed on the other mesh response curve.

Finally, dynamic transmission error spectral contents are analyzed on the spur gear set (no profile modification, pitch errors of Figure 32). The corresponding spectra at 300 and 1200 rad/s on pinion are presented in Figures 34(a–d) and,

as in section 6.1, only the clearly identified components are commented. The most important amplitudes are attributed to the rotational frequencies (Nf_1, Nf_2, Nf_3) and the mesh frequency and its harmonics (Nfm), some harmonic combinations ($f_1 + f_2$) and numerous side-bands ($Nfm \pm (f_1 - f_2)$, $Nfm \pm f_1$, $Nfm \pm f_2$) emerge after filtering. Contrary to the type A gear unit, the three rotational frequencies appear in the transmission error signals of stages 1 and 2.

7. CONCLUSION

A modular and systematic formulation is proposed in order to include the contributions of tooth shape modifications and mounting errors to single and double stage geared system dynamic behaviours. The corresponding elementary matrices and vectors combined with some classical finite elements and lumped parameter elements can account for deformable shafts, bearings and time-varying, possibly non-linear, mesh stiffnesses and excitation functions. The state equations are solved by using the Iterative Spectral Method presented in reference [23] which is adapted to a 3D gear mesh interface model and multi-mesh geared set dynamics including combined multi-frequency parametric and external excitations. As far as stiff non-linearities such as total contact losses are not considered, results of the modified Iterative Spectral Method compare well with those delivered by a time-step integration technique combined to a normal contact algorithm for highly reduced computational times. Such a procedure allows extensive parametric analyses that could hardly be conducted by using time-step methods. From a practical point of view, it is shown in this paper that double mesh systems with an idler gear (type B) exhibit stronger dynamic couplings than double stage systems of the type A. In particular, the limitation of the definition of tooth shape modifications on a stage by stage basis is pointed out.

The development of more refined models of gear elastic characteristics (convective effects on tooth flanks, gear blank flexibility, . . .) and the experimental validation of the proposed methodology are some of the necessary extensions of the present work.

REFERENCES

1. H. N. Özgüven and D. R. Houser 1988 *Journal of Sound and Vibration* **121**, 383–411. Mathematical models used in gear dynamics—a review.
2. G. W. Blankenship and R. Singh 1992 *American Society of Mechanical Engineers, Proceedings of the 6th International Power Transmission and Gearing Conference, Phoenix* **1**, 137–146. A comparative study of selected gear mesh interface dynamic models.
3. P. Velex 1993 *Comportement dynamique et acoustique des transmissions par engrenages, chapter* 2, *CETIM*, 39–95. Modélisation du comportement dynamique des transmissions par engrenages.
4. G. V. Tordion and R. Gauvin 1997 *Transactions of the American Society of Mechanical Engineers, Journal of Engineering for Industry* **99**, 785–791. Dynamic stability of a two-stage gear train under the influence of variable meshing stiffnesses.

5. H. IIDA and A. TAMURA 1984 *Proceedings of the Conference on Vibrations in Rotating Machinery*, *Institution of Mechanical Engineers*, 67–72. Coupled torsional–flexural vibration of a shaft in a geared system.
6. H. IIDA, A. TAMURA and H. YAMAMOTO 1986 *Bulletin of the Japanese Society of Mechanical Engineers* **29**, 1811–1816. Dynamic characteristics of a gear train system with softly supported shafts.
7. F. K. CHOY, Y. K. TU, M. SAVAGE and D. P. TOWNSEND 1989 *American Society of Mechanical Engineers*, *Proceedings of the 5th International Power Transmission and Gearing Conference*, *Chicago* **1**, 383–387. Vibration signature analysis of multistage gear transmissions.
8. P. VELEX and A. SAADA 1991 *Proceedings of the Japanese Society of Mechanical Engineers International Conference on Motion and Power Transmission*, *Hiroshima*, 117–122. Modal analysis for the prediction of dynamic tooth loads in geared trains.
9. K. UMEZAWA, T. AJIMA and H. HOUJOH 1986 *Bulletin of the Japanese Society of Mechanical Engineers* **29**, 950–957. Vibrations of three axis gear systems.
10. P. VELEX and A. SAADA 1991 *Proceedings of the 8th International Federation for the Theory of Machines and Mechanisms World Congress*, *Prague* **2**, 621–625. A model for the dynamic behaviour of multi-stage geared systems.
11. H. LINKE and J. BÖRNER 1991 *Proceedings of the Japanese Society of Mechanical Engineers International Conference on Motion and Power Transmission*, *Hiroshima*, 31–36. Dynamic loads on gear trains with idler gears.
12. M. RASHIDI and T. L. KRANTZ 1992 *American Society of Mechanical Engineers*, *Proceedings of the 6th International Power Transmission and Gearing Conference*, *Phoenix* **1**, 347–358. Dynamics of a split torque helicopter transmission.
13. A. KAHRAMAN 1994 *Transactions of the American Society of Mechanical Engineers*, *Journal of Mechanical Design* **116**, 706–712. Dynamic analysis of a multi-mesh helical gear train.
14. A. KAHRAMAN 1994 *Transactions of the American Society of Mechanical Engineers*, *Journal of Mechanical Design* **116**, 713–720. Planetary gear train dynamics.
15. A. SAADA and P. VELEX 1995 *Transactions of the American Society of Mechanical Engineers*, *Journal of Mechanical Design* **117**, 241–247. An extended model for the analysis of the dynamic behavior of planetary trains.
16. P. VELEX and L. FLAMAND 1996 *Transactions of the American Society of Mechanical Engineers*, *Journal of Mechanical Design* **118**, 7–14. Dynamic response of planetary trains to mesh parametric excitations.
17. T. E. ROOK and R. SINGH 1995 *Journal of Sound and Vibration* **182**, 303–322. Dynamic analysis of a reverse-idler gear pair with concurrent clearances.
18. H. VINAYAK, R. SINGH and C. PADMANABHAN 1995 *Journal of Sound and Vibration* **185**, 1–32. Linear dynamic analysis of multi-mesh transmissions containing external, rigid gears.
19. G. W. BLANKENSHIP and R. SINGH 1995 *Mechanism and Machine Theory* **30**, 43–57. A new gear interface dynamic model to predict multi-dimensional force coupling and excitation.
20. H. VINAYAK and R. SINGH 1996 *American Society of Mechanical Engineers*, *Proceedings of the 7th International Power Transmission and Gearing Conference*, *San Diego*, 535–541. Linear dynamic analysis of multi-mesh transmissions containing external, compliant gears.
21. H. VINAYAK and R. SINGH 1998 *Journal of Sound and Vibration* **210**, 171–214. Multi-body dynamics and modal analysis of compliant gear bodies.
22. P. VELEX and M. MAATAR 1996 *Journal of Sound and Vibration* **191**, 629–660. A mathematical model for analyzing the influence of shape deviations and mounting errors on gear dynamic behaviour.
23. J. PERRET-LIAUDET and J. SABOT 1991 *Proceedings of the 8th International Federation for the Theory of Machines and Mechanisms World Congress*, *Prague* **1**, 213–216. Dynamics of gears. A method for computation of vibration spectra.

24. J. PERRET-LIAUDET 1996 *Journal of Sound and Vibration* **196**, 165–177. An original method for computing the response of a parametrically excited forced system.
25. J. PERRET-LIAUDET and J. SABOT 1995 *Pub. LMA No.* 142, *Proc. 1er colloque G.D.R. Vibro-acoustique*, *Marseille*. Résolution des grands systèmes d'équations différentielles à coefficients périodiques: application aux transmissions par engrenages.
26. H. N. ÖZGÜVEN and D. R. HOUSER 1988 *Journal of Sound and Vibration* **125**, 71–83. Dynamic analysis of high speed gears by using loaded transmission error.
27. J. P. RACLOT 1997 *Thèse de Doctorat*, *INSA de Lyon*. Analyse de la réponse dynamique de trains d'engrenages à simple et double étage de réduction avec écarts de forme par une méthode spectrale itérative (in French).
28. M. MAATAR and P. VELEX 1996 *Transactions of the American Society of Mechanical Engineers*, *Journal of Mechanical Design* **118**, 586–589. An analytical expression of the time-varying contact length in perfect cylindrical gears. Some possible applications in gear dynamics.
29. M. LALANNE and G. FERRARIS 1990 *Rotordynamics—Prediction in Engineering*. New York: John Wiley and Sons.
30. R. G. MUNRO 1962 *PhD Thesis*, *Cambridge University*. The dynamic behaviour of spur gears.
31. R. W. GREGORY, S. L. HARRIS and R. G. MUNRO 1963 *Proceedings of the Institution of Mechanical Engineers* **178**, 261–266. Dynamic behaviour of spur gears.
32. P. VELEX, M. MAATAR and M. OCTRUE 1995 *Proceedings of the 2nd Institution of Mechanical Engineers International Conference on Gearbox Noise and Vibration*, 199–208. Loaded transmission error predictions and measurements on spur gears with profile reliefs.
33. P. VELEX 1995 *Thèse d'Habilitation à Diriger des Recherches*, *INSA de Lyon-Université Lyon* I. Dynamique de l'Engrenage (in French).
34. R. W. CORNELL 1981 *Transactions of the American Society of Mechanical Engineers*, *Journal of Mechanical Design* **102**, 447–459. Compliance and stress sensitivity of spur gear teeth.
35. DRAFT INTERNATIONAL STANDARD ISO/DIS 6336-1.2 1990, 87–95. Calculation of load capacity of spur and helical gears. Part I: basic principles and influence factors.
36. P. SAINSOT 1990 *Thèse de Doctorat*, *INSA de Lyon*. Analyse du contact entre dentures d'engrenages cylindriques de réducteurs (in French).
37. A. KUBO, K. YAMADA, T. AIDA and S. SATO 1972 *Bulletin of the Japanese Society of Mechanical Engineers* **38**, 2692–2715. Research on ultra high speed gear devices.

APPENDIX: MAIN NOTATIONS

$\hat{A}_{12}$	angle between the centre lines of stages 1 and 2
C_{int}, C_{out}	input, output torque
c_α	modal damping coefficient associated with the αth modeshape
$e_s(M^*)$	maximum normal gap in the base plane of stage s
f_1, f_2, f_3	rotational frequency of shaft 1 (input), shaft 2 (intermediate), shaft 3 (output)
f_m	mesh frequency
f_{m1}	mesh frequency stage 1
f_{m2}	mesh frequency stage 2
$f_z(t)$	defined in equation (23)
$\Im x$	spectrum imaginary part amplitudes
I_{ps}, I_{gs}	pinion, gear transverse moment of inertia
I_{ops}, I_{igs}	pinion, gear polar moment of inertia
J_k	polar moment of inertia of the kth shaft line
k_{si}	stiffness of the ith cell in the base plane of stage s (Figure 2)
k_{ms}, $\Delta k_s(t)$	average and time-varying component of stage s mesh stiffness

k_α average modal stiffness associated with the αth modeshape
m_{ps}, m_{gs} mass of stage s pinion, gear
m_α modal mass associated with the αth modeshape
M^* a point of contact in rigid-body conditions
$N_{cs}(t)$, $N_s(t)$ actual and nominal time-varying number of contacting cells in the base plane of stage s
$Nstage$ number of stages
$p_{1s}(M_i)$ distance from a potential point of contact M_i to pinion (Figure 2)
$p_{2s}(M_i)$ distance from a potential point of contact M_i to gear (Figure 2)
q_s degree-of-freedom vector of the pinion-gear pair of stage s
Rb_{ps}, Rb_{gs} base radii of stage s pinion, gear
$\Re x$ spectrum real part amplitudes
$SF(TE)$ shape factor of transmission error
$TE_i(\omega)$ ith frequency content of transmission error
T_{ms} mesh period of stage s
T_1 mid-point of the tangent between base plane and pinion base cylinder (Figure 2)
T_2 mid-point of the tangent between base plane and gear base cylinder (Figure 2)
u_{ps}, v_{ps}, w_{ps} pinion translational degrees of freedom (stage s)
u_{gs}, v_{gs}, w_{gs} gear translational degrees of freedom (stage s)
$V_s(M_i)$, V_{ms} structure vector in M_i, average structure vector of stage s
α_{ps} apparent pressure angle (stage s)
β_s, β_{bs} helix angle, base helix angle (stage s)
δ vector of the unknowns in the pseudo-modal basis
$\delta e_s(M_i)$ normal gap at M_i, potential point of contact in the base plane of stage s
ϕ_{ps}, Ψ_{ps}, θ_{ps} pinion rotational degrees of freedom (stage s)
ϕ_{gs}, Ψ_{gs}, θ_{gs} gear rotational degrees of freedom (stage s)
λ_{ps}, λ_{gs} angular position of the pinion, gear eccentricity (Figure 4)
$\eta_s(M_i)$ co-ordinate of a potential point of contact M_i along the line of contact (equation (7) and Figure 2)
ρ_1, ρ_2 percentages of modal strain energy on mesh 1 and 2, respectively
$\Delta_s(M_i)$, $\Delta_{so}(M_i)$ deflection at M_i, quasi-static deflection at M_i, (stage s)
Ω_{int}, Ω_{out} input, output rigid-body angular velocity
Ω_{ps}, Ω_{gs} pinion, gear rigid-body angular velocity (stage s)
$\bar{A}$ vector A completed by zeros to the total system size
$^{\mathrm{T}}A$ transpose of A (matrix or vector)